INL/EXT-21-63805
Revision 0

Post-Irradiation Examination of Legacy High Burnup Fuel to Support Safety Testing

September 2021

Fabiola Cappia, Tsvetoslav Pavlov, David Frazer, Kaustubh Bawane, Fei Teng, Boopathy Kombaiah, and Walter Williams
Idaho National Laboratory

INL is a U.S. Department of Energy National Laboratory
operated by Battelle Energy Alliance, LLC

INL/EXT-21-63805
Revision 0

Post-Irradiation Examination of Legacy High Burnup Fuel to Support Safety Testing

Fabiola Cappia, Tsvetoslav Pavlov, David Frazer, Kaustubh Bawane, Fei Teng, Boopathy Kombaiah, and Walter Williams

September 2021

Idaho National Laboratory
Characterization and Advanced PIE Division
Idaho Falls, Idaho 83415

http://www.inl.gov

Prepared for the
U.S. Department of Energy
Office of Nuclear Energy
Under DOE Idaho Operations Office
Contract DE-AC07-05ID14517

Page intentionally left blank

ACKNOWLEDGEMENTS

The authors would like to acknowledge J. Stanek, B. Frickey, S. Haney, M. Cook, and B. Miller for performing the sample preparation in Hot Fuel Examination Facility and IMCL. We would also like to thank Chester Perry, Chad Cole from the Radioprotection Staff, and the EML operation staff for technical support during the micromechanical testing. We are indebted to J. Merrill, M. Hunt, J. Skinner, and K Williams for administrative support to the project.

CONTENTS

FIGURES

TABLES

Page intentionally left blank

ACRONYMS

ATF	Accident Tolerant Fuels
EBSD	Electron Backscattered Diffraction
EDS	Energy Dispersive Spectroscopy
EML	Electron Microscopy Laboratory
EPMA	Electron Probe Micro Analysis
FEG	Field Emission Gun
FIB	Focused Ion Beam
HAADF	High-angle annular dark-field imaging
HAGB	High-Angle Grain Boundaries
HBS	High Burnup Structure
IMCL	Irradiated Materials Characterization Laboratory
IPF	Inverse Pole Figure
IQ	Image quality
KAM	Kernel Average Misorientation
LAGB	Low Angle Grain Boundaries
LHGR	Linear Heat Generation Rate
LOCA	Loss of Coolant Accident
LWR	Light Water reactor
PBS	Polarizing beam splitting
PFIB	Plasma Focused Ion Beam
RIA	Reactivity Initiated Accident
SAED	Selected Area Electron Diffraction
SEM	Scanning electron microscope
TCM	Thermal conductivity microscope
TEM	Transmission electron microscope

Page intentionally left blank

Post-Irradiation Examination of Legacy High Burnup Fuel to Support Safety Testing

1. INTRODUCTION

Safety/transient testing to evaluate performance under off-normal conditions is an essential pillar for both the development of Accident Tolerant Fuels (ATF) and the optimization of fuel operation economics beyond current discharge burnups. Among other factors, the successful interpretation of the transient testing results relies upon the knowledge of the initial conditions of the test, including the characteristics of the fuel system under scrutiny. When testing pre-irradiated material, the assumptions that the fuel and the cladding still have the same properties as in the pre-irradiation stage is obviously wrong and could affect the results of the test. This is particularly true for high burnup fuels. The knowledge of the initial microstructure of both fuel and cladding allows a clearer interpretation of the subsequent transient testing results, provides validation of the physical phenomena underlying the model predictions, and eliminates the uncertainties related to the limited knowledge of the sample status before the test. One example is the phenomenon of fine fragmentation that occurs in light-water reactor (LWR) fuel. During a Loss of Coolant Accident (LOCA) or Reactivity Initiated Transient (RIA) the fuel pellet can severely fragment [1, 2]. During LOCA, high burnup fuel tends to finely fragment, which has raised safety concerns due to the increased likelihood of dispersal of such small fuel particles once the cladding has burst and due to the increased fission gas release [3]. Therefore, efforts have been devoted to the assessment of the pulverization threshold that could determine the conditions under which fine fragmentation is predominant [4–8]. However, the lack of information regarding the initial conditions of the fuel and the connections between those conditions and the pre-transient irradiation history have hindered the development of a fully mechanistic fragmentation and pulverization criterion. The empirical relationships rely on conservative estimations due to the lack of information on critical material properties and characteristics [6, 9]. More generally, experimental evidence of the irradiation-induced modifications at microstructural scale are necessary to determine the behavior of the material at the macroscopic scale, with the latter being the one of technological interest. Significant progress has been made in the last two decades in the developments of analytical materials science techniques that can be applied to highly radioactive materials, such as high burnup fuels. The availability of new techniques and the improvement of existing ones have enabled investigations previously not possible that can deepen the understanding of the fuel characteristics and properties at high burnup. The better knowledge of material behavior and irradiation-induced phenomena could help the prediction of its performance. In this context, the scope of the present work is to apply a wide portfolio of advanced characterization techniques to determine properties that are relevant for safety and performance. The results are interpreted in the context of engineering scale post-irradiation examinations and available information on the irradiation conditions.

2. MATERIALS AND EXPERIMENTAL TECHNIQUES

2.1 Rod and Fuel Characteristics

The rods were irradiated for four cycles between 1997 and 2004, and segments of two of the original rods were tested in Severe Accident Test Stations at ORNL [7]. Table 1 summarizes the burnup accumulation of the assembly and of a lead rod [10], as well as the derived approximate Linear Heat Generation Rate (LHGR) of a representative lead rod. The rod and pellet characteristics are reported in Table 2. A sample from the rod with highest burnup and one from the rod with lowest burnup were selected to undergo further advanced examinations. The samples used for the advanced characterization was reprepared from the original ceramography specimens, which were cut at 283 mm from rod bottom within the high- power region of the respective rods.

Table 1. Operating history of the assembly and of a representative lead rod.

Cycle Number	Equivalent Full Power Days (EFPD)	Assembly Average Burnup (GWd/tHM)	Lead Rod Burnup (GWd/tHM)	Lead Rod LHGR (W/cm)
1	452.0	22.4	24.1	~240–260
2	508.6	46.4	48.1	~220–240
3	497.1	52.5	56.4	~60–70
4	451.2	67.6	71.8	~160–170

Table 2. Rod and pellet characteristics.

Pellet diameter (mm)	8.2
Initial enrichment (wt% U-235)	4.2
Fuel initial density (%TD)	94.89
Cladding outer diameter (mm)	9.5
Cladding material	M5®

2.2 Experimental Techniques

The advanced PIEs were performed at the Irradiated Materials Characterization Laboratory (IMCL) and at the Electron Microscopy Laboratory (EML).

Scanning Electron Microscopy images were collected using a Thermo Fischer Helios Plasma Focused Ion Beam (PFIB) and processed with the Maps 3.0 software. The image of the quarter pellet was created by stitching images acquired at 500×. A subsection of the sample spanning along the entire fuel and cladding radius was acquired at higher magnification to perform the quantitative image analysis. The images were cut radially at interval corresponding to radial steps of $r/r_0 = 0.01$ to quantify the porosity. The backscattered images offered enough contrast to segment the pores using a region-based clustering algorithm built-in in MATLAB®. Influence of grain pull-out and cracking of the surface in the porosity determination was minimized by excluding objects with high elongation and area exceeding 30 μm^2 from the quantification. The segmentation resulted in a binary image dividing pores and matrix phase from which statistics of the pores in 2D was determined as a function of the radius. Once the binary images have been created, a conservative estimation of the experimental error in determining the pore edges was given by expanding and contracting the pore masks by a line of pixels, which resulted in an upper and lower bound of the radial porosity value. Electron Backscattered Diffraction (EBSD) orientation maps were collected using the EDAX Hikari Super EBSD detector of the PFIB. The data processing was done using the EDAX OIM, Version 8 software.

The PFIB was used to coarse cut TEM lamellae at different radial positions. The final lamella preparation and thinning to TEM transparency was done in steps following different combinations of voltage and current, specifically: 30 kV/3nA–30k V/1nA–30 kV/0.5nA till final cleaning with 8 kV/77pA– 5kV/48pA using a Thermo Fischer Ga Quanta 3D Field Emission Gun (FEG) dual-beam Focused Ion Beam (FIB) system.

A Thermo Fischer Titan Themis 200 X-FEG TEM equipped with a Super-X Energy Dispersive Spectroscopy (EDS) system was used for semi-quantitative chemical analysis and imaging of the lamellae. Selected Area Electron Diffraction (SAED) data were collected to perform crystallographic analyses. The indexing of the SAED patterns was performed using the Crystallographic Toolbox CrysTBoX [11].

An Alemnis standard assembly equipped with the high-temperature module was used for the elevated temperature nanoindentation and nanoindentation creep experiments on the sample. The Berkovich cubic boron nitride (cBN) tip was calibrated on fused silica to measure the area function before the experiments. In addition, indents were performed on known other materials (tungsten and silicon) to check the accuracy of the area function. The sample was encased in a high-temperature cement after removal from the epoxy. The sample encased in the high-temperature cement was then mounted to a high-temperature stage of the Alemnis indenter using silver paste. The sample was then loaded into the Alemnis indenter using long reach tools and the indenter was loaded in a TESCAN LYRA 3 SEM/FIB instrument at EML. The stages of the Alemnis were then used to align the sample and the tip. Fields of indents were performed at variety of radii along the length of the pellet. The indents were performed at room temperature: 373 K, 573 K, and 773 K. The loading scheme for the indents was to load to 100 mN at 10 mN/s followed by a hold period and then the indents were unloaded at 10 mN/s. The length of the hold period following the loading was temperature dependent. A hold time of 20 s was used for room temperature measurements. Hold times up to 45–60 s for 773 K. The hold period was increased with temperature to minimize the plastic deformation, thus enabling the measurement of the reduced modulus. At the temperatures of 573 K and 773 K nanoindentation creep experiments were also performed. In the nanoindentation creep experiments the indent was loaded to 100 mN at 10 mN/s and the hold period was 300 s. The sample was then unloaded at 10 mN/s. The 300-s hold was used to enable the capture of both first and second stage creep in the samples. The linear second stage portion of the creep curve is used to calculate the stress exponents of the material. The sample and tip were heated independently at 10 K/min to the desired temperature for the high-temperature nanoindentation and nanoindentation creep experiments. The thermal drift between the tip and the sample was minimized with test indents and a temperature offset measurement. The drift was measured to be below the 0.15 nm/s during the nanoindentation and nanoindentation creep experiments.

For the thermal property measurements, two techniques were employed: a laser-flash method and the thermal conductivity microscope (TCM), a new technique based on the thermoreflectance method [12–14] . Thermal diffusivity values were measured as a function of temperature using a NETZSCH LFA427 instrument. The layout of this laser-flash system is shown in Figure 1a. This laser-flash system has been customized for remote operation inside of a shielded glovebox facilitating the handling of highly radioactive nuclear materials [12]. The samples' dimensions were measured using a micrometer in the hot cells. The sample is placed in a sapphire holder held in place by two alumina components (see Figure 1b), which are then placed inside a furnace. It is then heated to a desired temperature under a high-purity argon atmosphere under a pressure of 1.1 bars. After reaching equilibrium, the front surface of the specimen is subjected to a short laser pulse (0.6 ms to 1.2 ms). The rear surface temperature response is recorded via an infrared detector as a function of time. This transient temperature response is also calculated using an analytical or numerical solution of the heat equation. Thermal diffusivity is evaluated by minimizing the least square difference between the measured and calculated transients.

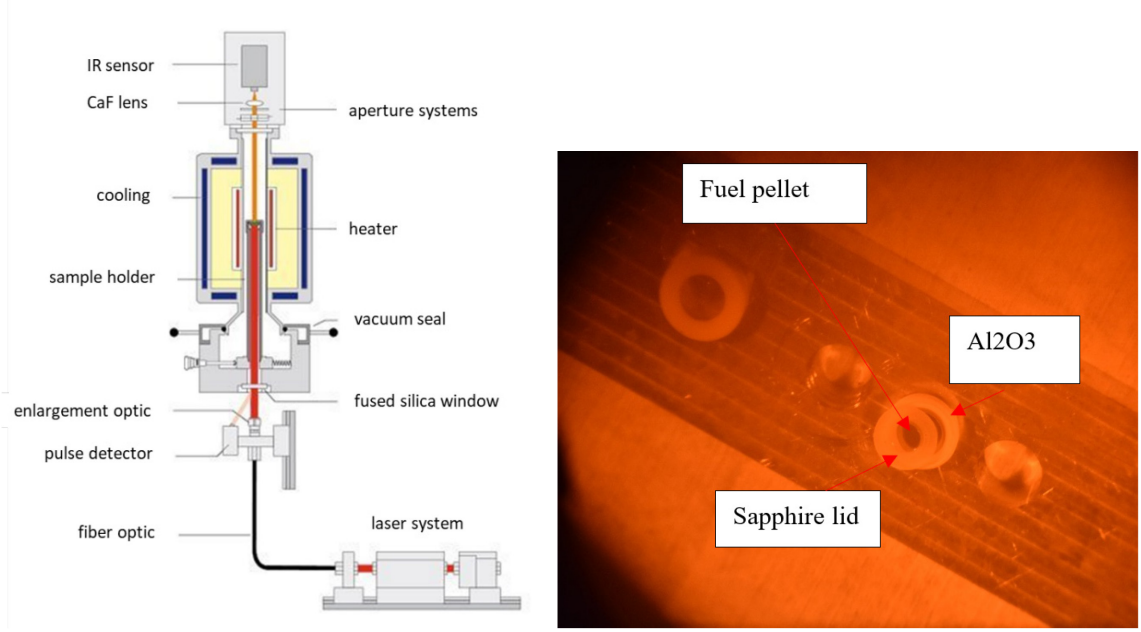

(a) (b)

Figure 1. (a) Layout of the NETZSCH LFA system. (b) Overview of the slice of fuel mounted in the sapphire cup and alumina holder before closure of the containers.

The TCM layout is shown in Figure 2. The sample is potted in a metallographic mount and polished to a high-quality surface finish. The polished sample is then sputter coated alongside a transparent borosilicate crown glass (BK7) sample. The BK7 gold film thickness is measured via an in-house developed laser device[15]. Gold's reflectivity is very sensitive to temperature changes at around 532 nm (high coefficient of thermoreflectance in absolute terms), which makes it a good candidate for probing the temperature response along the sample surface. The pump and probe are continuous wave lasers that operate at 660 nm and 532 nm, respectively. The pump laser, as the name suggests, serves as a periodic heat source which is subjected to sinusoidal modulation via a function generator. The pump laser light is passed through a set of lenses, reflected off a short-pass dichroic mirror and focused via an objective onto the sample surface. The probe laser beam is p-polarized via a half-wave plate and transmitted through a polarizing beam splitting (PBS) cube. It is then reflected via a long-pass mirror, circularly polarized via a quarter-wave plate, and focused onto to the gold-coated sample surface. The reflected probe beam is, then, passed again through the quarter-wave plate and transformed into s-polarized light. It is reflected off the long-pass mirror and then reflected by the PBS onto the photodetector. The voltage reading produced by the photodetector is passed through a pre-amplifier and, finally, the periodic thermal response signal is extracted via a lock-in amplifier. The pump laser is initially focused away from the probe. It is, then, incrementally moved towards the probe beam until they become coincidental. At every location the thermal response measured by the detector is recorded and a phase difference between the reference (pump) and detected (probe) phases is calculated. This process is repeated at different separation distances between the pump and the probe lasers and at a range of modulation frequencies (1 kHz to 100 kHz). The probe beam is scanned using a pair of Newport VP-25XA stages and a Newport ESP301 controller. The phase difference is simultaneously calculated via a numerical solution to the three dimensional, two-layer transient heat transfer problem [16]. An optimization algorithm is employed to determine thermal diffusivity and thermal conductivity by minimizing the least squares difference between the model output and experimental data. The method and equipment has been previously extensively tested on standard reference materials such as CaF_2, ZnS, ZnSe, and fused SiO_2 [14,17].

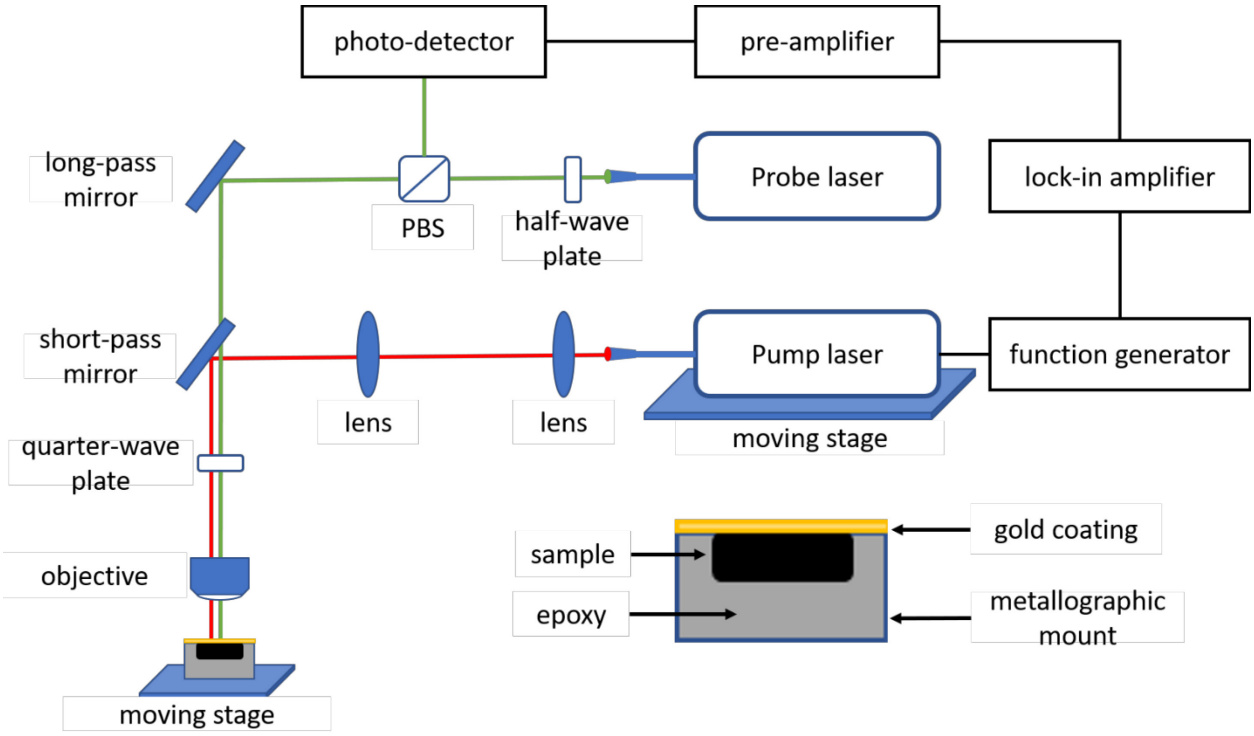

Figure 2. Experimental layout of the TCM.

3. PIE RESULTS

The primary objective of these investigations was the assessment of the microstructural status of the fuel at the end of the base irradiation, to support the interpretation of safety test results, both current and planned. However, the microscale PIE results must be interpreted in the context of the overall rod performance at the engineering scale, hence the results of the historical PIE executed previously are reported first. The data collected on the microstructure have then been combined with the measurements of mechanical and thermal properties presented in the following sections.

3.1 Historical PIE

All the rods underwent non-destructive examinations, which included visual inspection, profilometry, neutron radiography, gamma scanning and eddy current measurements. The results of that testing campaign were already presented and discussed in Ref. [10], and they are here only briefly recalled. Compared to the Zr-4 rods, the M5® rods had excellent visual appearance, exhibited low corrosion, with the maximum oxide thickness being less than 25 µm with no sign of breakaway, and little irradiation-induced growth. The neutron radiography highlighted that at a few axial locations pellet-pellet gaps larger than expected (see white arrow in Figure 3), but no enhanced formation of hydrides occurred at those axial positions. Afterwards, the rods were punctured, and the amount of released fission gas was determined based on the series of backfill and expansions. The results of the fission gas release measurements are reported in Figure 4, together with literature data from high-power rods for comparison [18]. The burnup was obtained using wet chemistry methods and Inductively Coupled Plasma Mass Spectrometry (ICP-MS). Comparison of the calculations with the measured local burnup is shown in Table 3, showing good agreement between the two. Using the local burnup measurements, the axial burnup profile of the rods was obtained by scaling the ^{137}Cs gross gamma counts, assuming a conversion factor between the counts and the measured burnup value at the specific axial location (Figure 5). Cladding hydrogen measurements were conducted at different axial locations (Figure 6a) using a LECO®

RH-404 Hydrogen analyzer modified for remote operation in a laboratory hood. The hydrogen pick up had a moderate increase towards the upper portion of the fuel rod, consistently with higher local cladding temperature. Overall, the hydrogen content remained low (Figure 6b), and the measured values for rod average burnup >70 GWd/tHM confirm the low hydrogen pick up fraction of M5® cladding [19, 20].

The original ceramography images of the samples from the highest and lowest burnup rods (Rod A08 and Rod P16, respectively) are shown in Figure 7 and Figure 8. In both fuels, three major areas can be seen along the radius, represented by the three high-magnification images reported in Subfigures b–d of the two figures. In both samples, the central region, extending till approximately mid-radius, exhibited a medium density of pores. The pore shape is more irregular for the specimen from A08 and more round for the other specimen. In the A08 specimen metallic precipitates decorate the pores, which appear as white spots under the optical microscope in Figure 7b. Those do not appear in the central region of the sample from P16, probably because they are under the resolution limit of the optical microscope. For both samples, the porosity dropped past the mid-radius, (Figure 7c and Figure 8c). In the outer radius region, there was a high density of small pores, typical of the formation of the High Burnup Structure (HBS), as visible in Figure 7d and Figure 8d. At the fuel cladding interface, an internal oxidation layer (seen as a uniform color of light gray contrast) of nominally 10–15 μm was present in both samples, which is the bonding layer forming between UO_2 and the oxidized cladding characterizing high burnup fuels.

Table 3. Local burnup measurements compared to the burnup calculations for the four rods.

Rod ID	Measured local burnup* (GWd/tHM)	Predicted Burnup (GWd/tHM)
A08	76.87	75.08
B16	72.66	72.86
D05	70.06	76.25
P16	66.86	67.26

* The burnup is calculated from the measured Nd-148 concentration and assuming a conversion factor between Fission of Initial Metal Atoms (% FIMA) to GWd/tHM of 9.42 GWd/tHM/%FIMA.

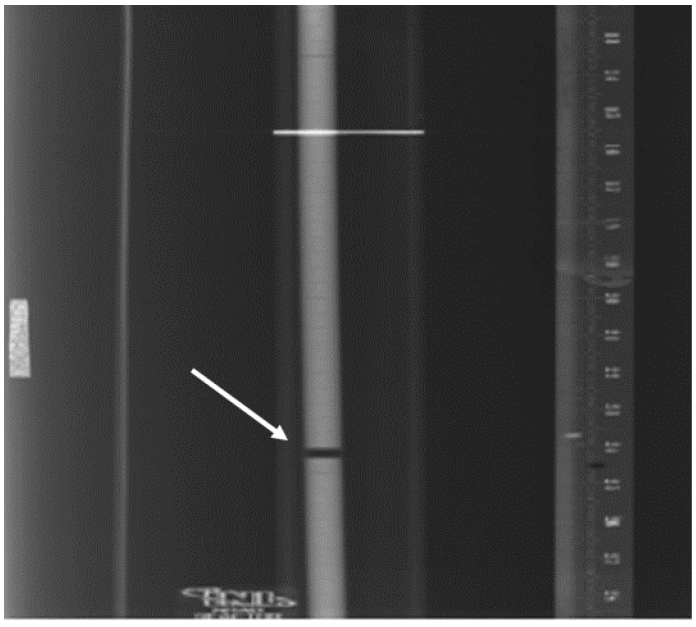

Figure 3. Example of neutron radiography of a rod portion, highlighting the abnormal pellet-to-pellet gap (see white arrow in the figure).

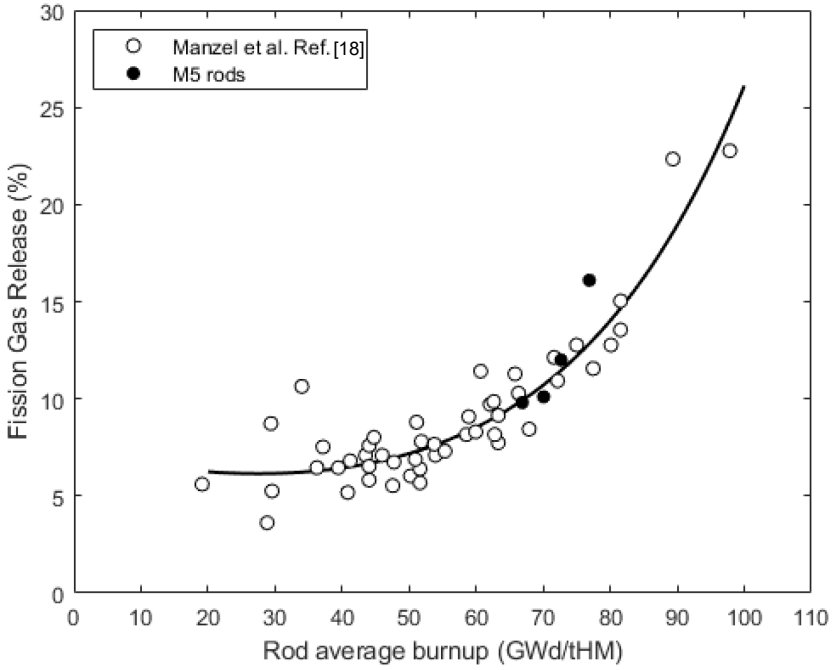

Figure 4. Measured fission gas release for the four M5 rods (black circles) compared to literature data for high-power rods (white circles).

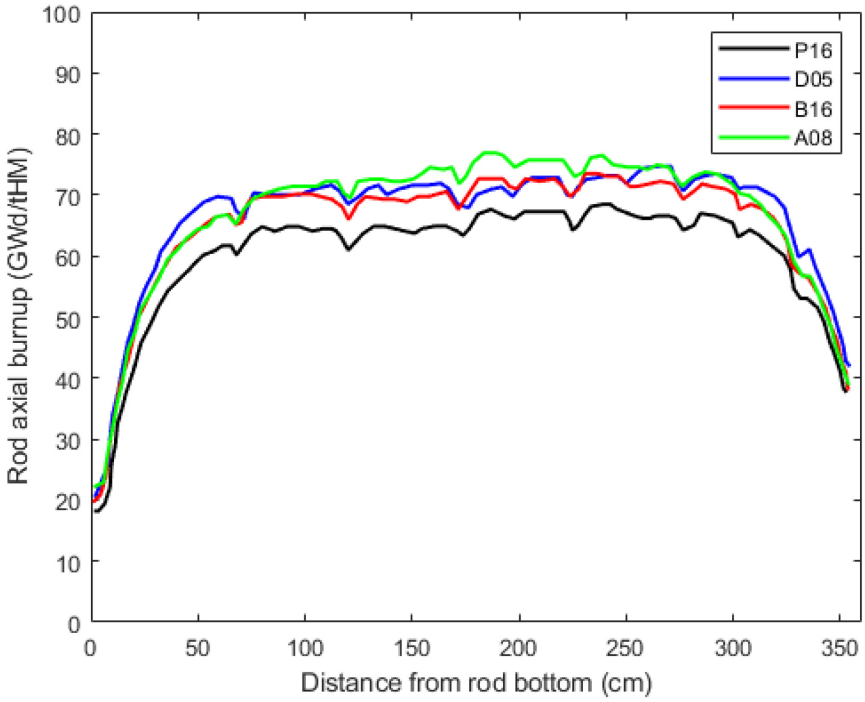

Figure 5. Axial burnup profile of the four rods obtained by scaling the gross ^{137}Cs activity with the local burnup measured via wet chemistry.

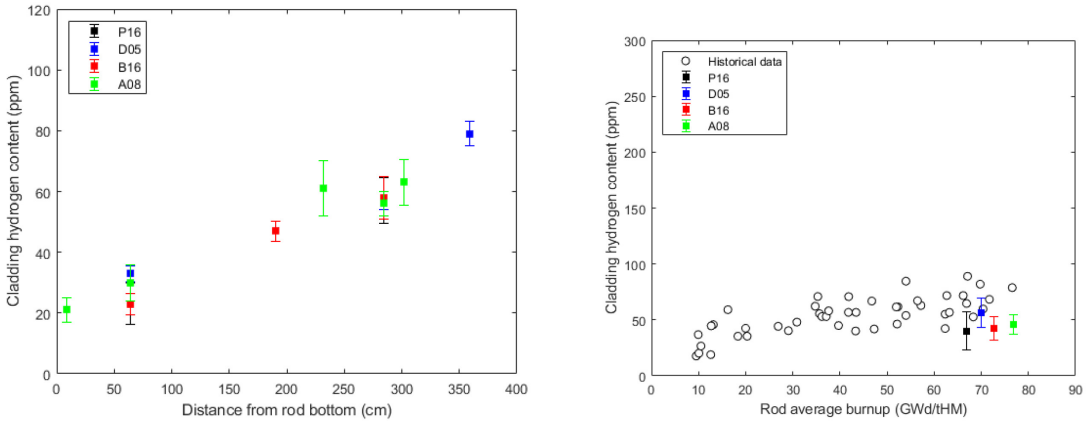

(a) (b)

Figure 6. (a) Measured cladding hydrogen content along the rod axis. (b) Comparison of the average value of cladding hydrogen content versus historical data from other M5 rods.

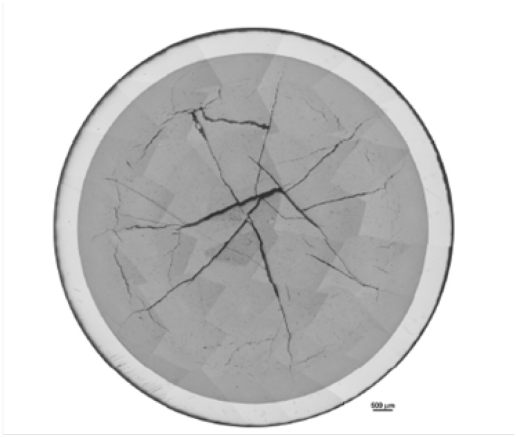

(a)

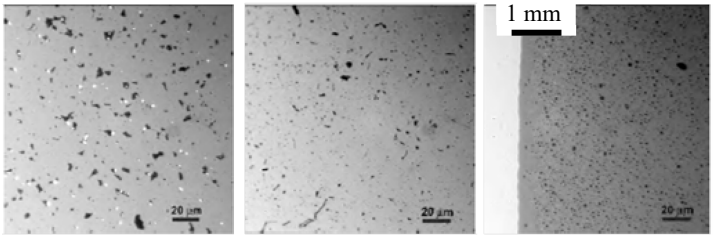

(b) (c) (d)

Figure 7. (a) Overview of the original fuel cross section from Rod A08. High magnification image of (b) fuel center, (c) fuel mid-radius and (d) fuel periphery and interaction with the cladding.

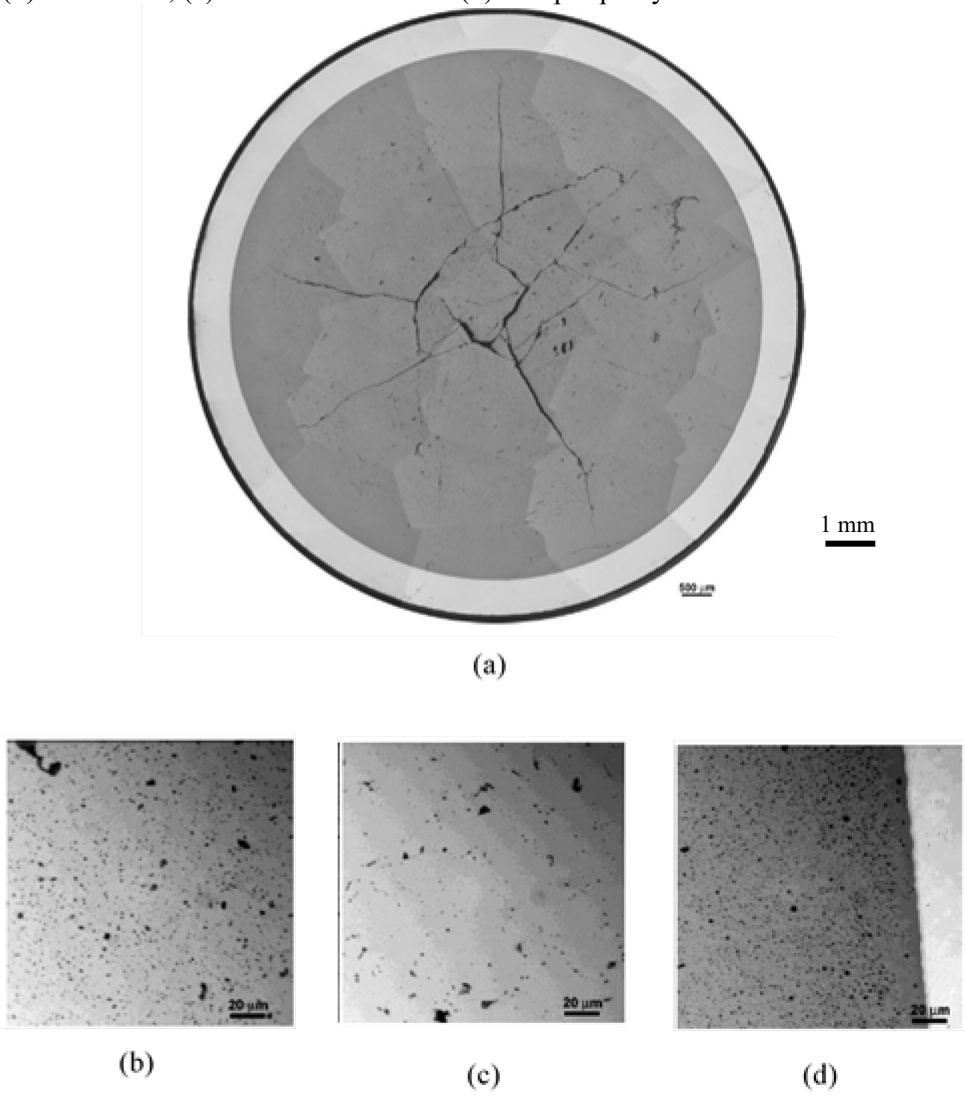

Figure 8. (a) Overview of the original fuel cross-section from Rod P16. High magnification image of (b) fuel center, (c) fuel mid-radius and (d) fuel periphery and interaction with the cladding.

3.2 Advanced PIE

3.2.1 Microstructural Examinations

The advanced microstructural examinations were focused on the sample from A08, which was reprepared, and subsized into a quarter pellet to reduce the overall dose from the sample and minimize damage to the detectors. Electron Probe Micro Analysis (EPMA) data had been previously collected on this specimen [21]. Some of those results are reproduced here due to their relevance in the interpretation of the present PIE results. Among the fission products, the noble gases are of particular interest, as the pressurized bubbles are one of the driving forces for fragmentation [5]. The radial distribution of Xe is shown in Figure 9. Up to mid-radius, all the gas has been released. The measured Xe concentration reaches rapidly the produced amount past $r/r_0 \approx 0.50$ and it decreases again towards the periphery. The signal drops to 0.2–0.4 wt% and is very scattered, which suggests that most of the gas is trapped in the

increased porosity at radial positions exceeding r/r_0=0.8. Indeed, the X-ray maps collected at the fuel periphery show that the bubbles are filled Figure 10). The radial profiles of other two volatile fission products, Cs and Te, are shown in Figure 11. As for Xe, depletion of Cs and Te is noticeable in the fuel center till r/r_0=0.50. Past the mid-radius, the Cs concentration approaches 0.6wt%, which is approximately the amount created. An increase in both Cs and Te is visible at the outermost pellet peripheral positions (r/r_0>0.95), reflecting the local burnup increase, but the contribution of some radial migration from the center cannot be excluded.

The two-dimensional porosity radial profile is shown in Figure 12, which confirms the qualitative trend observed with the optical microscope. Three major zones across the fuel radius can be identified: a first region from fuel center to $r/r_0 \approx 0.55$ characterized by porosity values 2–4%, a second zone from $r/r_0 \approx 0.55$ till $r/r_0 \approx 0.80$ with low porosity and a third zone that covers the rest of the fuel radius with a rapid increase in porosity typical of the HBS formation, both in transition and fully developed [22]. In addition to the porosity, the pore mean area and two-dimensional pore number density are presented in Figure 13. The data shown in Figure 13 allow for further analyses of the pore characteristics. In the central region, the porosity is due to a limited number of cavities with large size, above 1 μm^2. The pores are irregular not only in shape (see Figure 7b), but also in size, as demonstrated by the large standard error of the pore mean area. Moving toward the mid-radius, the pore area tends to decrease, but the porosity remains constant due to the number increase occurring at mid-radius (r/r_0=0.50–0.55). Between r/r_0=0.60–0.80 both the mean size and the number density remain low, causing the porosity drop in Figure 12. Finally, the porosity increase is due to the number density increase as the mean area remains close to 1μm^2, which is a typical observation associated with the HBS [22]. The pores all have similar size in this zone, being the standard error of the mean very narrow (Figure 13).

In addition to the SEM imaging, EBSD maps were collected at selected radial locations to determine the grain structure and orientation. Image quality maps and inverse pole figure (IPF) maps are shown in Figure 14. From the fuel center to mid-radius, the original grains, separated by High-Angle Grain Boundaries (HAGB), are internally subdivided by Low Angle Grain Boundaries (LAGB).[1] In the IPF maps, the LAGB are shown by the white lines, while the HAGB are shown as black lines (see legend in Figure 14i). The internal subdivision can also be appreciated from the quality maps (Figure 14a, c, e), where the subgrains appear as darker lines within the grains, due to the local distortion they create in the diffraction patterns. The amount of LAGB increases moving from the center to mid-radius. At mid-radial position, a clear transition is visible, both in terms of porosity and grain structure. As can be appreciated in Figure 14e and f, the left side of the images (towards the fuel center) is characterized by a high density of small intragranular pores and subdivided grains, while on the right side of the images (towards the cladding) neither high density of pores nor grain subdivision is present. Moving towards the cladding, at the point of minimum porosity (i.e., at relative radial positions 0.70–0.75) the grain subdivision is absent (Figure 14g and h). Another way to visualize the characteristic of the microstructure from the EBSD data is presented in Figure 15, which shows Kernel Average Misorientation (KAM) maps. Albeit only qualitative, the maps help to highlight how the formation of the subgrains increases the local lattice distortion. The behavior is obvious by looking at Figure 15b, which corresponds to the IPF shown previously in Figure 14f. The left side shows a much higher degree of local misorientation across the entire structure, while on the right side, where the grains are not internally subdivided, the local distortion is confined mainly along the original grain boundaries. Figure 15a, which was taken at a relative radial position of 0.26 in the central region with internally subdivided grains resembles the right part of Figure 15b, whereas Figure 15c confirms the behavior observed outside the restructured region in Figure 15b.

[1] LAGB are grain boundaries with misorientation <15 degrees, while HAGB are grain boundaries whose average misorientation exceed 15 degrees [47].

TEM lamellae were extracted in the fuel center zone, at r/r_0=0.20–0.30, fuel mid-radius where the grain and porosity structure changed (see Figure 14e and f), at $r/r_0 = 0.73$ before the start of the restructuring and at the fuel periphery in the HBS. Each lamella was imaged in weak beam condition close to zone axis [011] to highlight the dislocation structure within the grains. Such imaging setting does not allow to determine the total dislocation density in the sample due to the invisibility criterion, but it allows for a comparison of the damage level at different radial locations. Examples are shown in Figure 16. Outside the HBS, entangled dislocation lines are the predominant type of defects present, but loops can be observed too (see white arrows in Figure 16a and b). The level of damage is substantial, making it difficult to distinguish the dislocation lines. The Ham's method was chosen to calculate the defect concentration and to compare the dislocation density to the literature values presented by Nogita et al. [23]. Results are reported in Figure 17, which shows that the measured values are in the same order of magnitude as the literature values. It should be noted that due to the high level of damage, it was hard to distinguish the dislocation lines, which are severely entangled. Therefore, it can be expected that the current values are underestimated. No significant differences were measured in the dislocation density for the four locations measured (i.e., fuel center, $r/r_0 = 0.20$-0.30, $r/r_0 = 0.50$-0.55 and $r/r_0 = 0.73$). The network of extended defects was not present in the recrystallized grains of the HBS, but small loops and defects can still be seen within the grains (see Figure 16c).

The optical microscopy already revealed the precipitation of metallic fission products whose size was of the order of a few microns in the central part of the fuel pellet. Presence of such precipitates, historically called ε-particle or five-metals precipitates [24], is a commonly observed feature in oxide fuels [25,26]. In addition to the metallic precipitates, large agglomerates containing predominantly Ba and Zr together with U were present at the pellet center. Examples are given in Figure 18a. In addition to Ba, Zr, U and O traces of Cs and Sr were also present in the Ba-rich precipitate (Figure 18b). SAED patterns could be obtained from the larger precipitate shown in Figure 18a. The perovskite cubic structure of $BaZrO_3$ (Pm-3m, n°221) was used to index the diffraction patterns, which returned a good fit. Other volatiles were associated to the large five-metals precipitates present in the fuel open porosity at the center, such as the Te agglomerate shown in Figure 19 at the top of the ε-particle. SAED patterns had excellent match with the trigonal structure of pure Te (space group $P3_121$ n° = 152 [27]), which is reported in the inset in Figure 19b. Fission products precipitates reaching micrometric size were present only in the central region of the fuel. Already at intermediate radius the size of the secondary phases was limited to tens to hundreds of nm, as can be seen in Figure 20 showing small particles within the grains and on grain boundaries at mid-radius. Similar observations were made on the extreme periphery of the fuel. In the TEM lamella extracted from the HBS, the micrometric bubbles have been opened during the lamella thinning and appear as holes (see for example Figure 16c). Nanometric bubbles were observed in each of the other lamellae, always decorated with ε-particles (Figure 20b, c, and d). Another example of intragranular bubble is shown in Figure 21a, which was imaged from the lamella taken in the unrestructured area at $r/r0 = 0.70$–0.80. The EDS map clearly shows that the cavity is filled with fission gas (Figure 21b). The bubble is surrounded by tangled dislocations, which appear as a dark region around the bubble in Figure 21a. On the right of the bubble, a plate-shaped defect was observed. The cavity is empty, but it may have contained gas at high pressure, as suggested by the tangled dislocation surrounding the defect. The origin of the defect is unknown, but the observation is similar to what shown by Thomas et al. [28], at comparable radial positions for another high burnup sample.

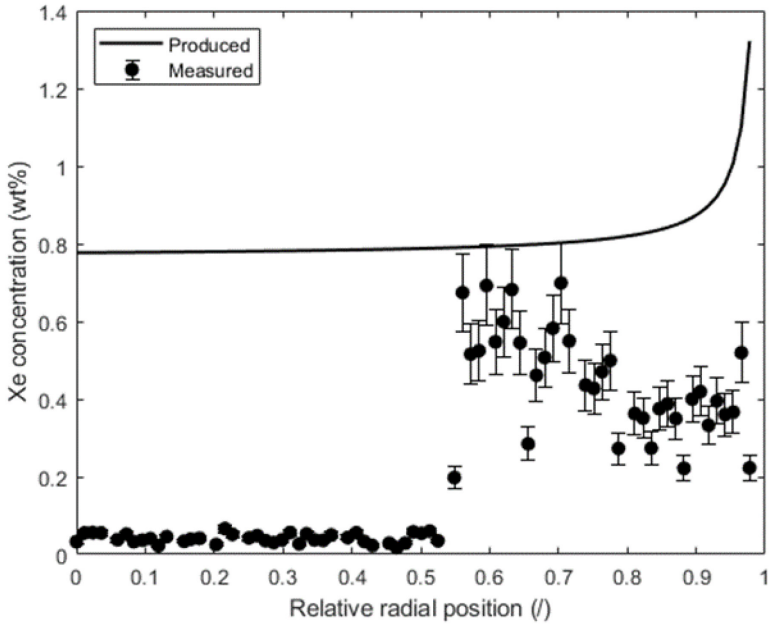

Figure 9. Radial distribution of Xe. Measured local concentration using EPMA (black circles) and predicted local concentration from estimated burnup (black solid line) [21].

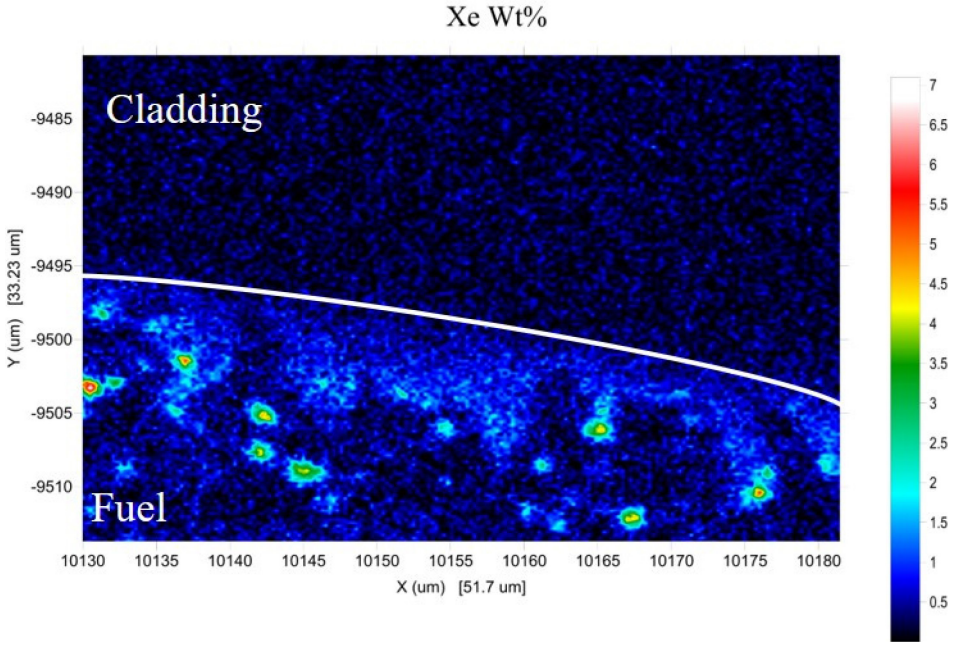

Figure 10. X-ray Xe map at the fuel periphery adjacent to the interaction layer with the cladding. The map highlights that the HBS bubbles under the sample surface are filled with fission gas [21].

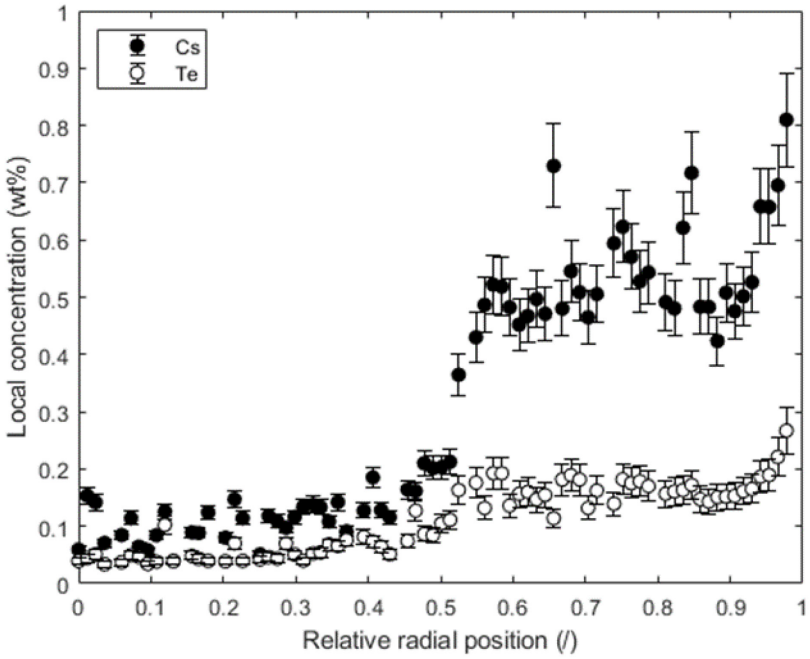

Figure 11. Radial distribution of Cs (black circles) and Te (white circles) [21].

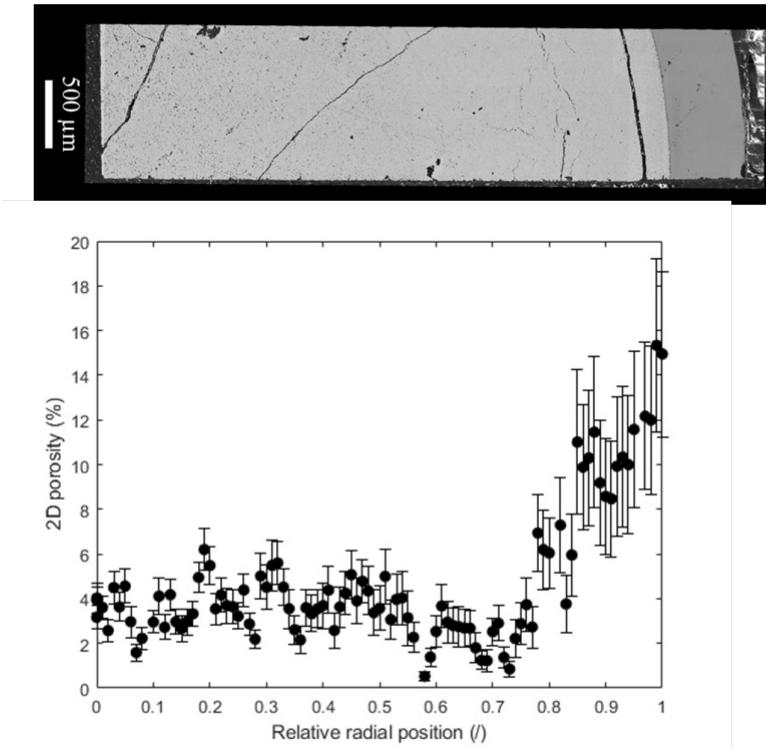

Figure 12. Porosity radial profile.

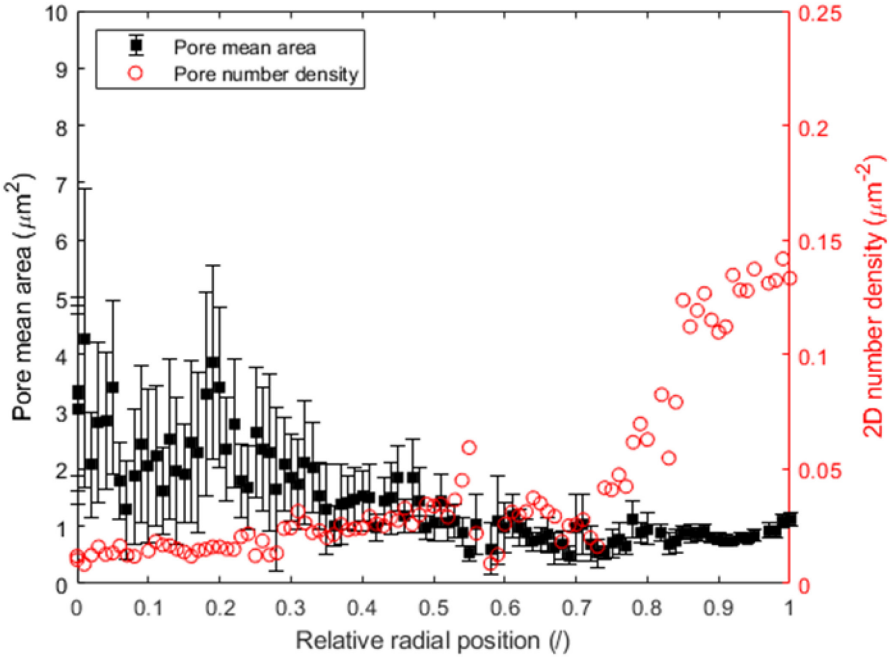

Figure 13. Pore mean area and 2D pore number density as a function of pellet radius.

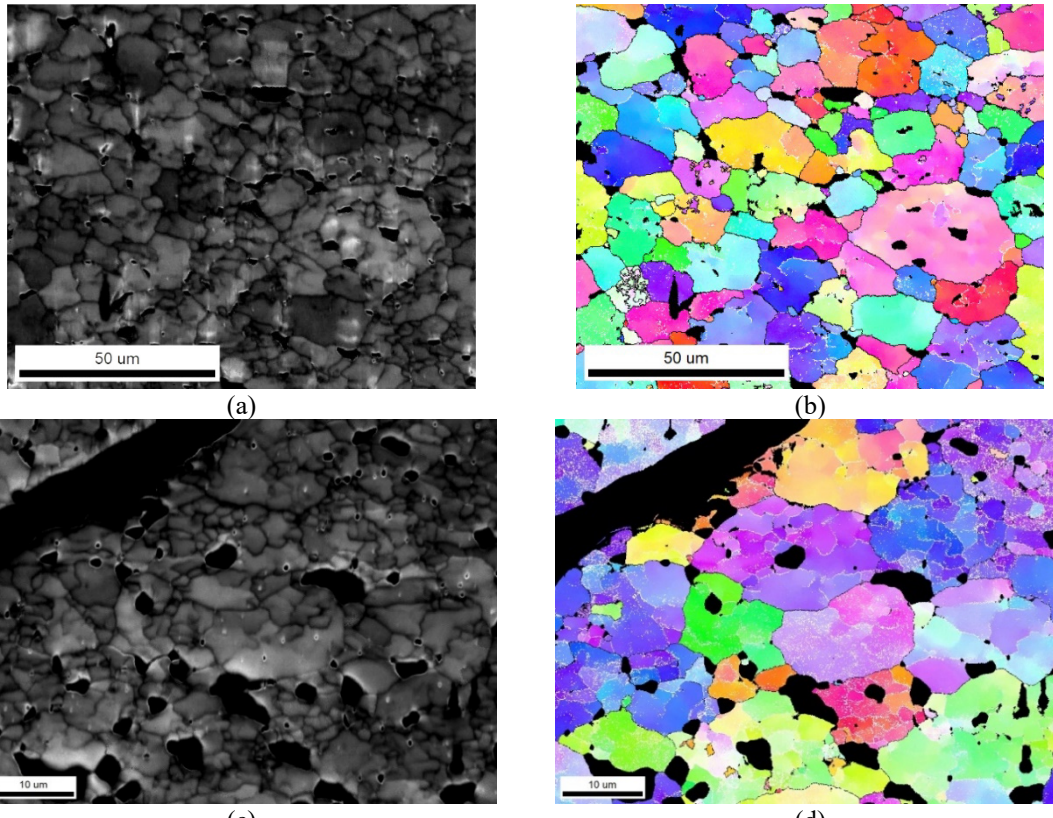

(a) (b)

(c) (d)

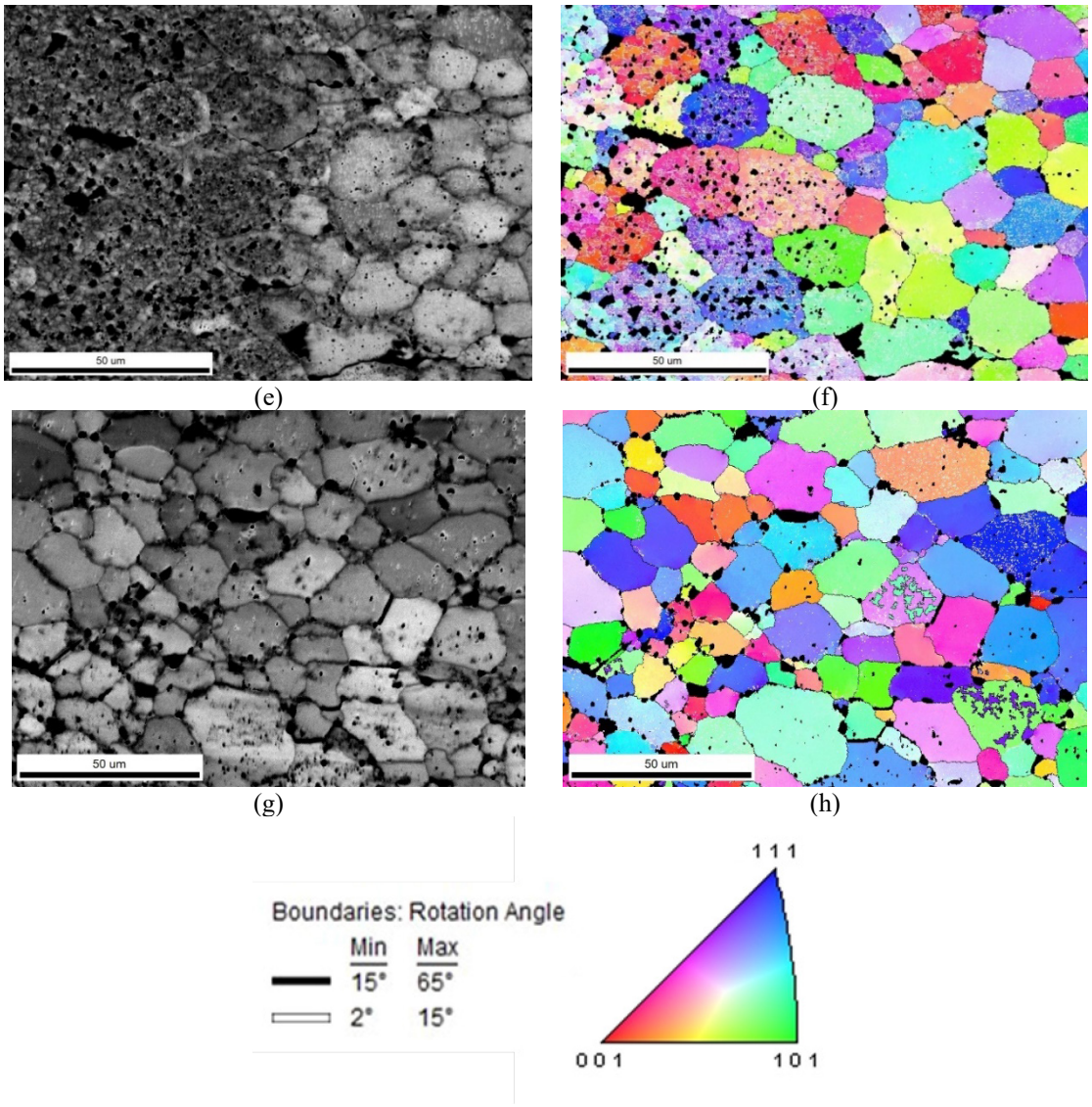

(e) (f) (g) (h) (i)

Figure 14. Image quality (IQ) and inverse pole figure (IPF) maps taken at different radial positions. (a)-(b) r/r0 =0.18, (c)–(d) r/r0 = 0.30 (e)–(f) r/r0 = 0.55–0.60 (interface between Zone 1 and 2), (g)–(h) r/r0 = 0.73-0.75. (i) IPF maps and grain boundary misorientation legend.

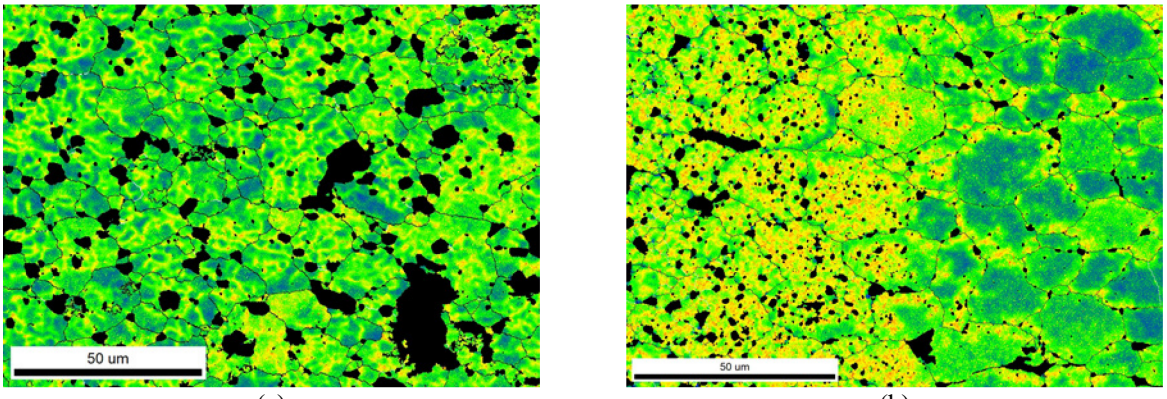

(a) (b)

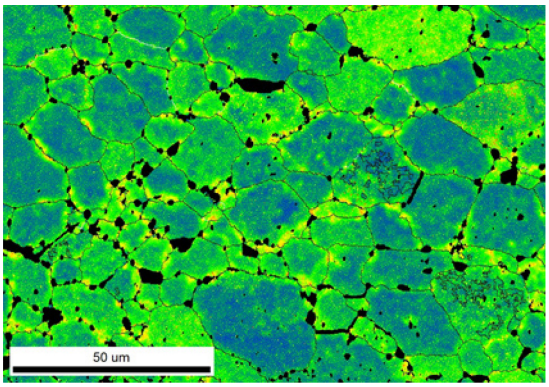

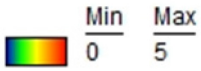

(c) (d)

Figure 15. Kernel Average Misorientation (KAM) maps taken at different radial locations. (a) r/r_0=0.26, (b) r/r_0=0.55, (c) r/r_0=0.73.

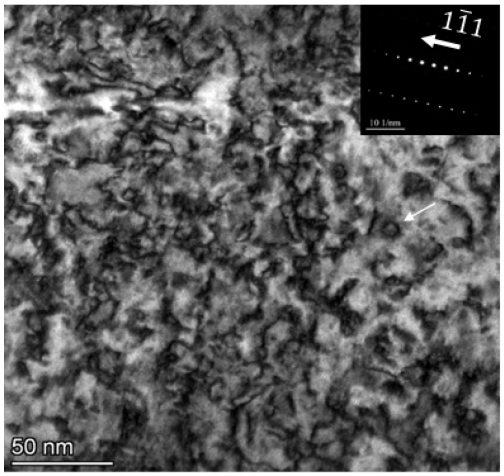

(a)

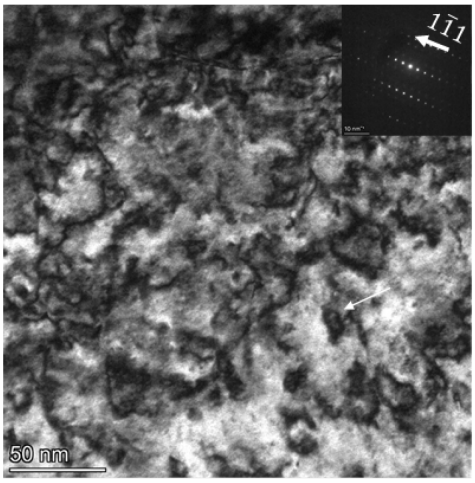

(b)

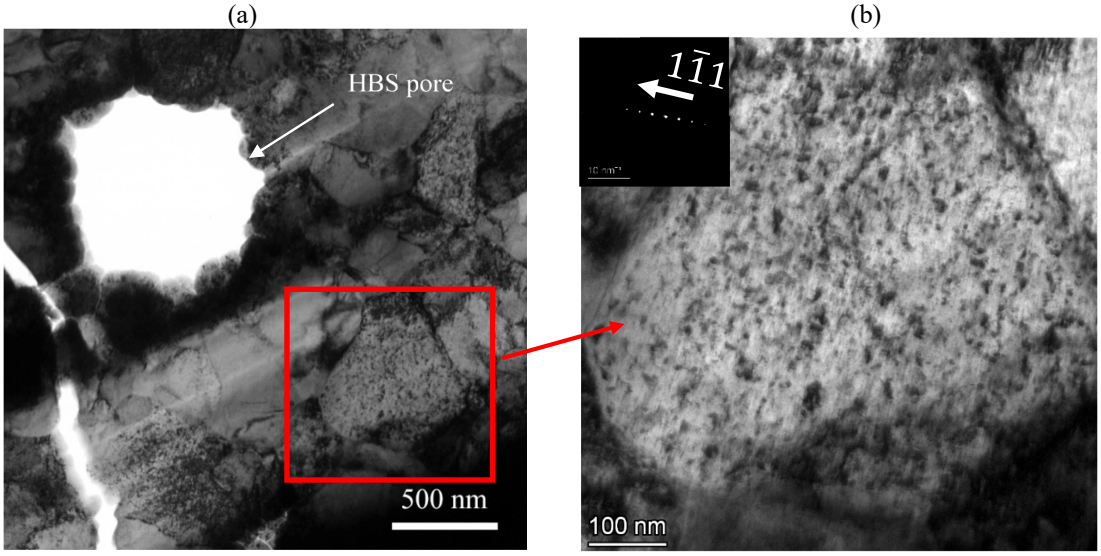

(c)

Figure 16. Bright Field TEM image showing intragranular dislocations (a) from the fuel center, (b) at mid-radius. The white arrows in (a) and (b) point to dislocation loops. (c) BF TEM image of multiple polyhedral grains in the HBS. The grain in the red box was tilted to weak beam condition. A magnification is shown on the right, where small loops can be seen.

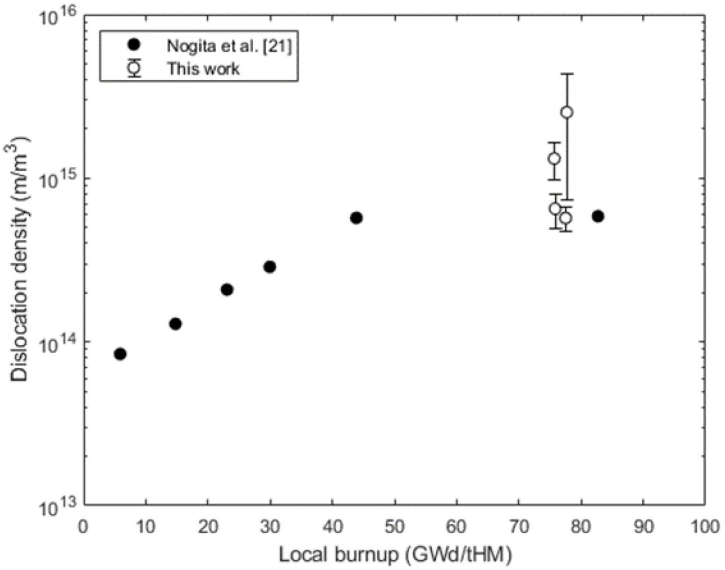

Figure 17. Dislocation density as a function of local burnup. The white circles represent the values reported by Nogita et al. [23], while the white circles are the values measured in this work at various radial locations outside the HBS.

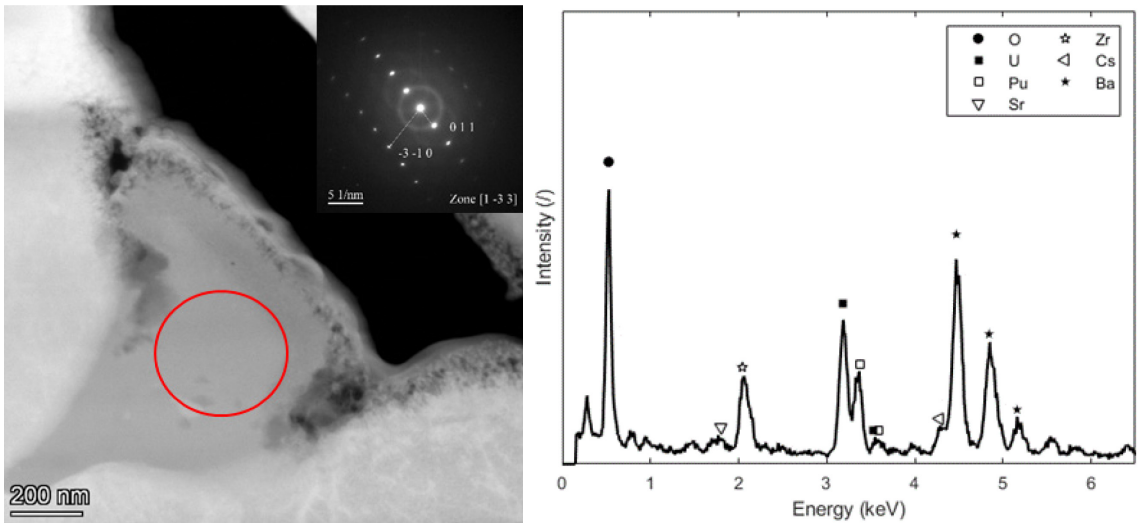

(a) (b)

Figure 18. (a) HAADF STEM image showing a large precipitate containing several fission products in oxide form. The red circle indicated the position of the SAED pattern shown in the inset in the figure. The structure agrees well with a perovskite cubic structure. (b) EDS spectrum of the precipitate in (a) showing the major components.

Table 4. Qualitative composition obtained from the EDS spectrum shown in Figure 18.

Element	Atomic concentration (at%)	Error (at%)
O	41.91	3.87
Zr	20.87	3.29
Ba	18.42	2.63
U	14.92	2.17
Cs	2.18	0.31
Sr	1.38	0.22
Pu	0.32	0.05

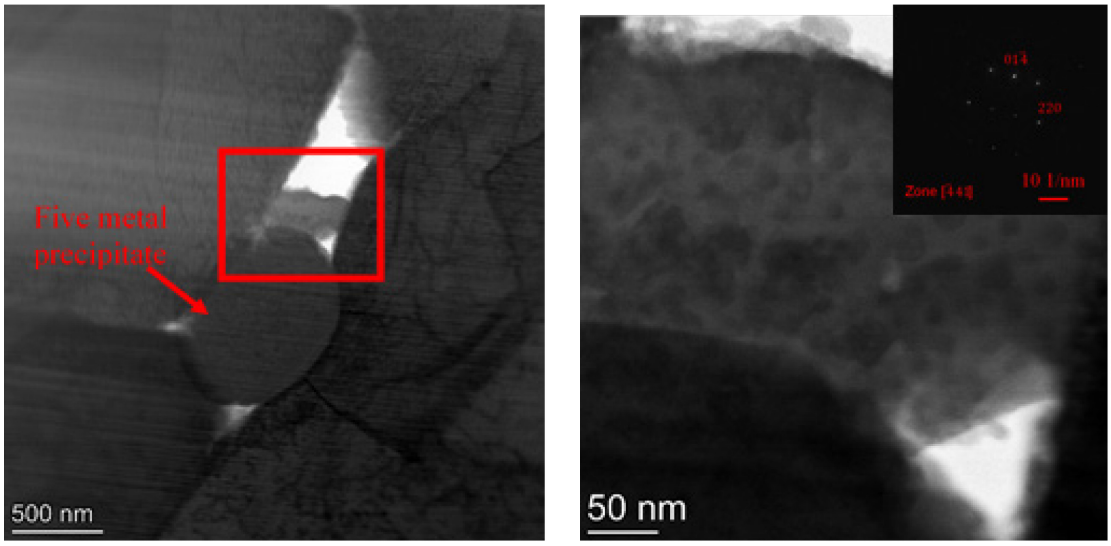

(a) (b)

Figure 19. (a) BF STEM image of a large intergranular five metal precipitate. On top of the precipitate another secondary phase agglomerate is present (red box), which is shown at higher magnification in (b). In (b) the top-right inset corresponds to the diffraction pattern from the Te precipitate.

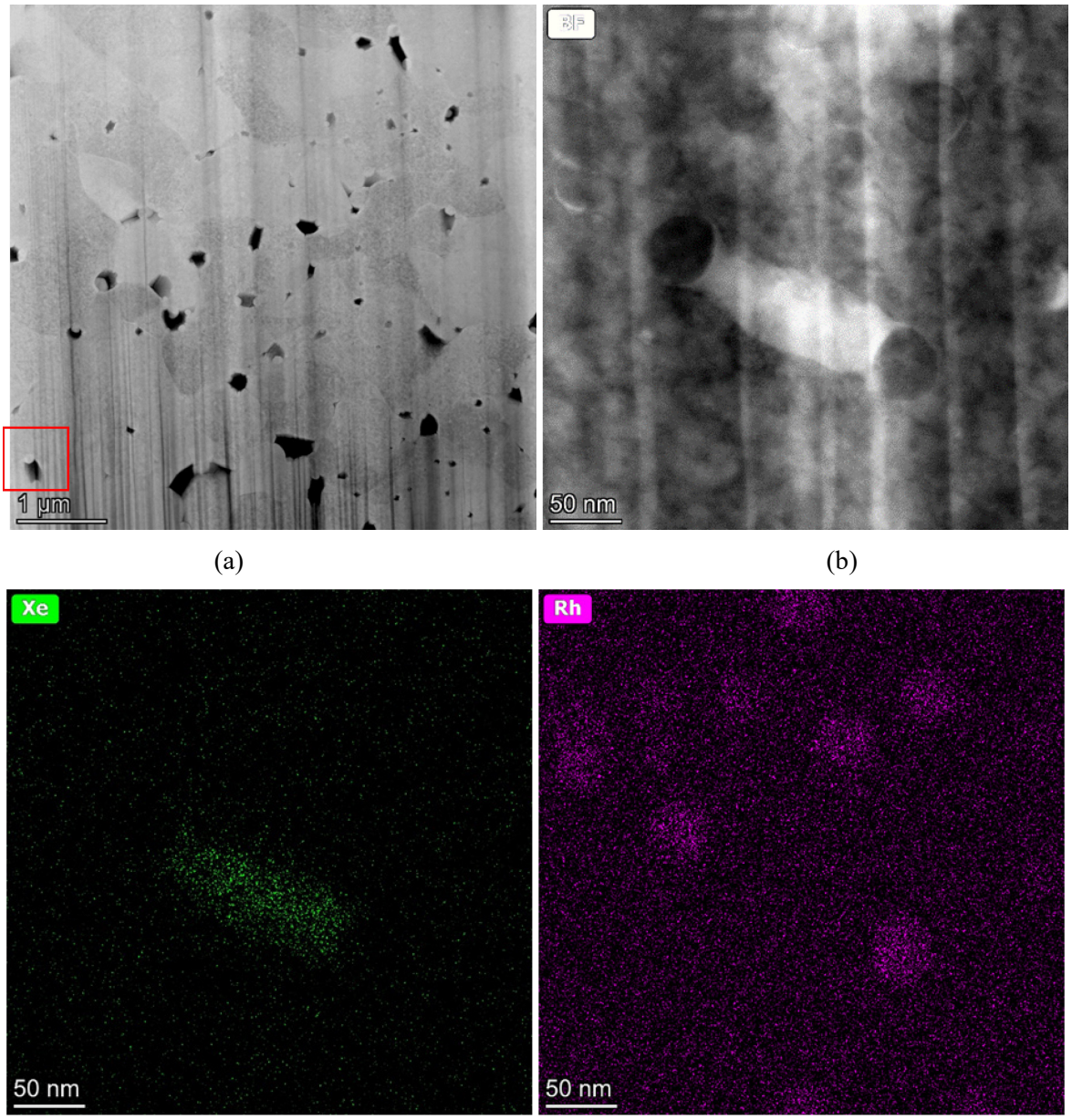

Figure 20. (a) HAADF image showing subgrain formed at mid-radius. (b) BF image of the red rectangle in (a) focusing on the fission products precipitates, (c) EDS atomic maps of (b) showing the Xe signal within an elongated bubble and (d) the nanometric five-metals precipitates within the subgrains decorating the fission gas bubble (only Rh is shown. Pd, Ru, Mo, and Tc showed the same behavior).

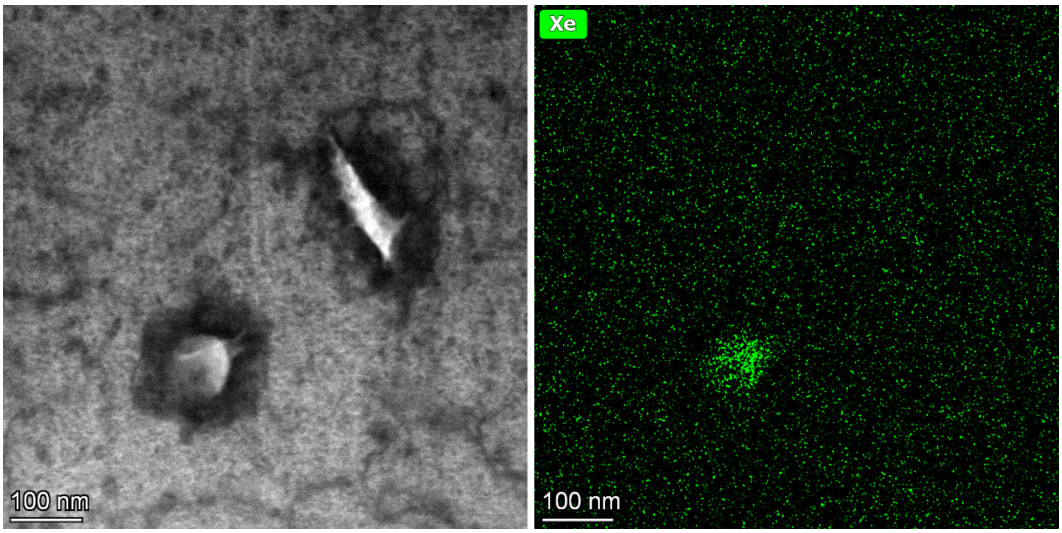

(a) (b)

Figure 21. (a) BF TEM image of intragranular cavities surrounded by dislocation tangles observed at radial position r/r0=0.70–0.80. (b) EDS map of the Xe signal, showing that one cavity is still filled with gas, while the plate-shaped one has released gas, probably during lamella thinning.

3.2.2 High-Temperature Micromechanical Testing

Nanoindentation or instrumented indentation can measure the Young's modulus, hardness, and creep properties of a material. The standard method for calibrating and analyzing the loading and unloading curve of a nanoindentation experiment was outlined by Oliver and Pharr [29]. A brief overview will be provided here, for a more detailed analysis see [29]. An example of a nanoindentation or instrumented indentation loading and unloading curve can be seen in Figure 22.

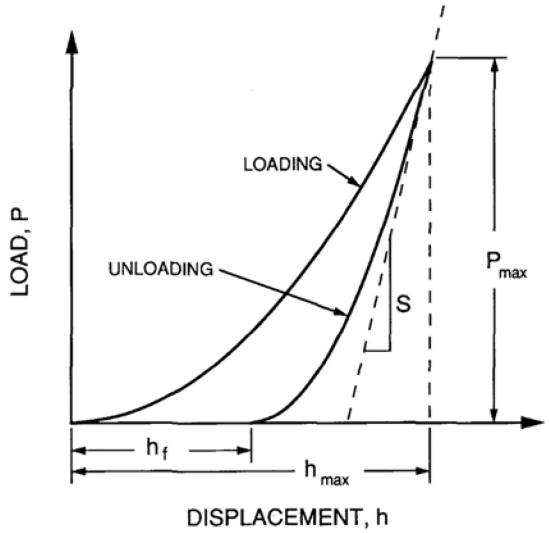

Figure 22. A schematic representation of load versus indenter displacement data for an indentation experiment. The quantities shown are Pmax: the peak indentation load; hmax: the indenter displacement at peak load; hf: the final depth of the contact impression after unloading; and S: the initial unloading stiffness [29].

The loading and unloading curves are then analyzed using Equation (1) for evaluating the reduced modulus of the material.

$$S = \frac{dP}{dh} = \frac{2}{\sqrt{\pi}} E_r \sqrt{A} \quad (1)$$

Where S (N/m) is the experimentally measured stiffness of the upper portion of the unloading data, E_r (Pa) is the reduced modulus and A (m^2) is the projected area of the elastic contact. The projected area of the elastic contact is evaluated using the area function of the tip. The calculation of the area function is explained in the next section. The reduced modulus is a system value that comes from the elastic deformation of the tip and the sample during the indentation test. To calculate the Young's modulus of the test specimen Equation (2) is used.

$$\frac{1}{E_r} = \frac{(1-\nu_s^2)}{E_s} + \frac{(1-\nu_i^2)}{E_i} \quad (2)$$

Where E_r (Pa) is the reduce modulus, ν_s (/) is the Poisson's ratio for the sample, E_s (Pa) is the Young's modulus of the sample, ν_i (/) is the Poisson's ratio for the indenter and E_i (Pa) is the elastic modulus of the indenter.

The hardness of the tested specimen is calculated with Equation (3).

$$H = \frac{P_{max}}{A} \quad (3)$$

Where H (Pa) is the hardness, P_{max} (N) is the max load during the indentation test, and A (m^2) is the projected area of elastic contact.

In nanoindentation the load frame compliance and the area function are important considerations for the experiments. Knowing the load frame compliance is necessary as the measured displacements during an indentation test are the sum of the displacements in the specimen and the load frame. Therefore, to accurately know the specimen displacements, the load frame compliance is needed. The load frame compliance can be found by modeling the load frame and the specimen as two springs in series. The specimen compliance during the elastic contact is given by the inverse of the contact stiffness, S, which can experimental be evaluated. Knowing the total compliance and using a specimen with a known compliance, the compliance of the load frame can be calculated. The area function of the tip is important since the computation of both the reduced modulus and the hardness depend on the contact areas. The method of calculating the area function of the indenter tip is based on the assumption that that the elastic modulus is independent of indentation depth [29]. A series of indents at different depths are made into a fused silica standard with a known hardness and Young's modulus which allow for the calculation of the tip area function. Since the elastic modulus and reduced modulus of the fused silica are known and the assumption that the elastic modulus and reduced modulus do not depend on depth it allows for fitting the data to calculate the area function.

Several fields of indents were performed at a variety of radial positions and temperatures in the irradiated UO_2, and the results can be seen in Figure 23. It can be observed that for both Young's modulus and hardness the values steady increase until approximately $r/r_0 \sim 0.5$ at which the values plateau until a value of $r/r_0 \sim 0.7$ and then the values start to decrease. The behavior inversely correlates well with the porosity profile measured by SEM (Figure 24).

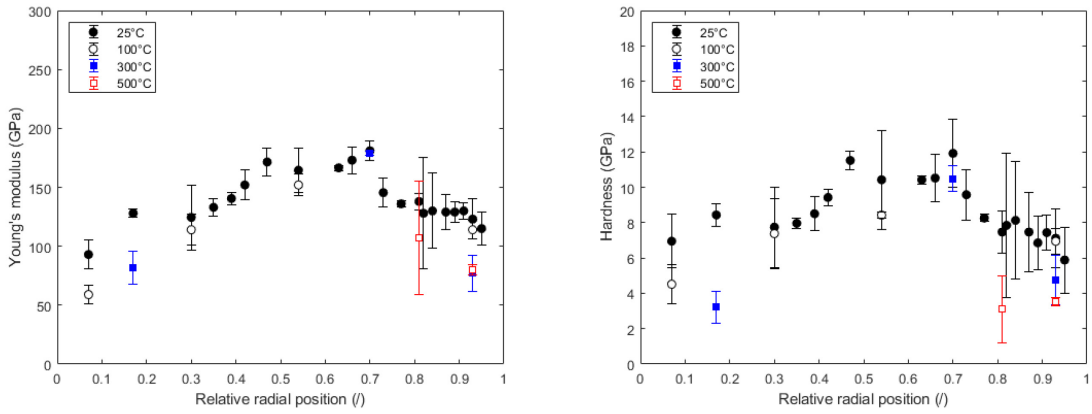

(a) (b)

Figure 23. (a) Young's modulus and (b) hardness as a function of the fuel radius, measured at different temperatures.

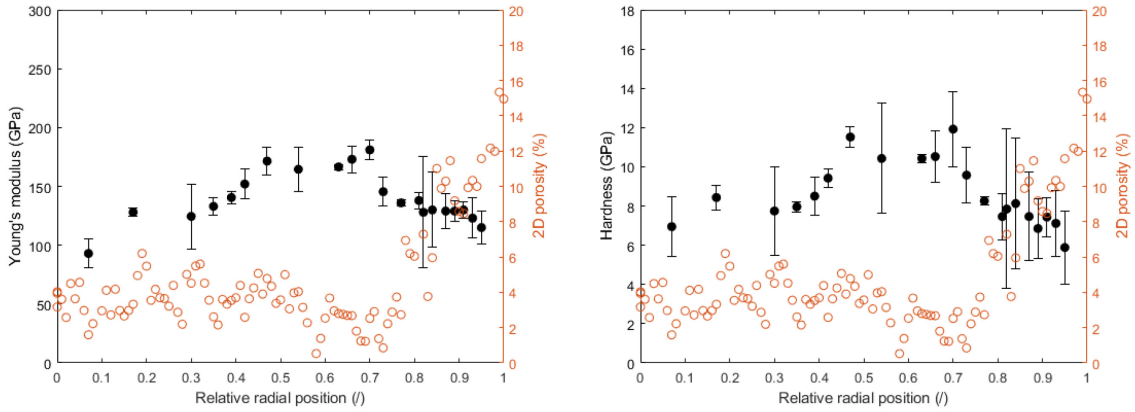

(a) (b)

Figure 24. (a) Young's modulus and (b) hardness as a function of the pellet radius, measured at room temperature (left axis). The profile of the two properties is compared with the measured local porosity (right axis).

The high-temperature studies were focused on the periphery of the pellet, as this is the portion of the fuel that operates at the temperatures that can be reached by the current experimental apparatus, thus the most relevant to understand the materials property during operation. Plots of the Young's modulus and hardness of the HBS over temperature are shown in Figure 25. In addition to the 100 mN indents at 300°C, 20-mN indents were also performed to evaluate the effect of the load in determining the Young's modulus and hardness. The higher load indents sample a larger volume of material which, combined with the high porosity of the fuel periphery, lead to the lower Young's modulus and hardness values. The lower load indents would sample a denser portion of the sample, which would lead to the higher values as seen in the plots. The data points obtained with a 100-mN load are considered more representative of the heterogeneous structure of irradiated specimens. It can also be seen in the figures that the measurements at room temperatures are affected by large standard deviation, when considering all the 49 indents performed. If the four lowest values (i.e., data points with <2 GPa of hardness and <60 GPa of reduced modulus) are discarded as being outliers, the deviation significantly decrease with little variation in the average value. It could be assumed that these indents were performed on pores or subsurface pores

affected the measurements, causing the extremely low values. It also believed that the porosity in the periphery is causing the large standard deviation in the results.

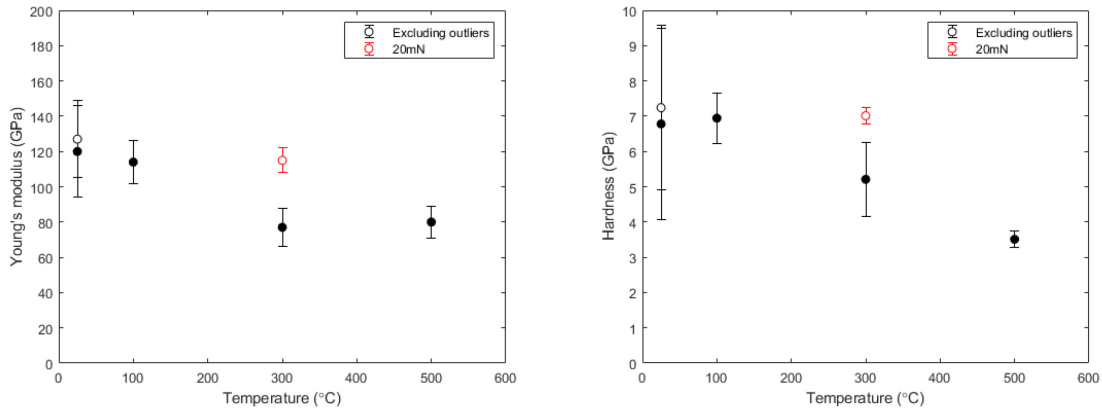

(a) (b)

Figure 25. (a) Young's modulus and (b) hardness as a function of temperature at the fuel periphery (r/r0~0.90–0.95).

3.2.3 Nanoindentation Creep Studies

The stress exponent of a nanoindentation creep experiment is calculated from the slope of ln(strain rate) and the ln(stress or hardness) curve [30,31]. This originates from the power-law creep equation for conventional steady-state creep which is shown in Equation (4).

$$\dot{\varepsilon} = A\sigma^n \tag{4}$$

Where n (/) is the uniaxial stress exponent and A is the uniaxial pre-exponential term, $\dot{\varepsilon}$ (s^{-1}) is the steady-state strain rate, and σ (Pa) is the stress for a uniaxial creep test.

The strain rate for nanoindentation creep experiments can be calculated with Equation (5):

$$\dot{\varepsilon}_i = \left(\frac{1}{h}\right)\left(\frac{dh}{dt}\right) \tag{5}$$

Where h (m) is the depth of the indent and *dh/dt* (m/s) is the penetration rate in the steady-state section or linear portion of the nanoindentation creep curve, which is assumed to correspond to secondary or steady-state creep. The stress during nanoindentation creep was calculated from the area of the tip and the force from the indenter or the hardness. In general creep testing values for n between 3–10 is considered the dislocation creep regime [30, 31]. When the stress exponent is large (n > 10) it is typically explained by introducing a "threshold stress" below which dislocation flow cannot be measured. Lastly, grain boundary sliding is usually occurring with a stress exponent between 1.5–2.5 [32] and diffusional creep has stress exponents of 1 [30, 31]. In Figure 26, a plot of the logarithm of both strain rate and stress for one of the creep tests at 500°C is shown with the linear fit to the data, which allow the estimation of the uniaxial stress exponent.

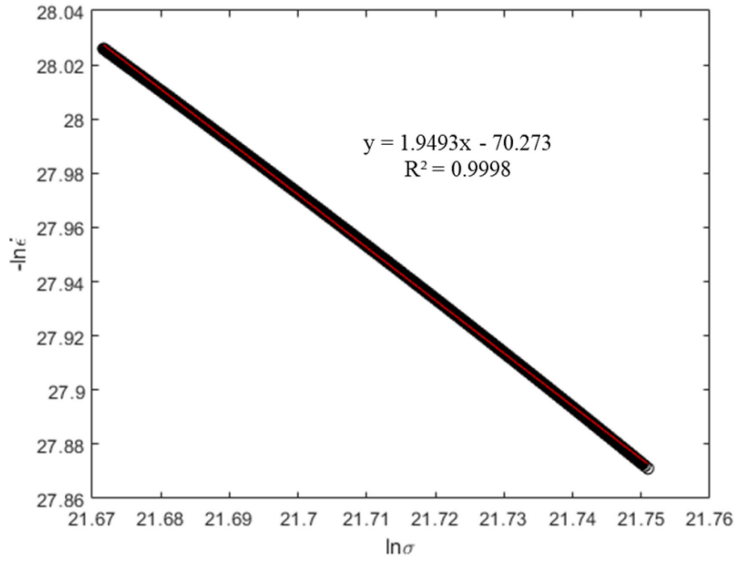

Figure 26. Ln($\dot{\varepsilon}$) versus ln(σ). The linear fit of the data is reported on the plot.

The stress exponents measured for the various tests are shown in Table 5. The stress exponents measure here would suggest that the center of the pellet and the HBS is deforming by dislocation glide in the material at 300°C. At 500°C the stress exponent measured would imply that the HBS is deforming by grain boundary sliding in the material.

Table 5. The stress exponents measure at the different locations and temperatures in the irradiated fuel.

Temperature (°C)	300	300	500
Pellet radial location	Center	Periphery	Periphery
Stress exponent	6.7 ± 2.4	2.8 ± 0.5	1.7 ± 0.4

3.2.4 Thermal Properties

The TCM measurements were conducted at room temperature on the same sample from Rod A08 that was used for the advanced microscopy and micromechanical testing. The results of the TCM measurements are shown in Figure 27 and Figure 28. The calculated thermal conductivity values have been obtained by using the measured thermal diffusivity in the first experimental campaign together with estimates for specific heat and density. The density was corrected for local porosity and matrix swelling due to nanometric bubbles and radiation induced defects. The porosity measurements in this work combined with an additional constant matrix swelling factor of 4% ± 1.5% (based on Spino et al. [33]) were used to calculate the density as a function of radius. Specific heat has been assumed invariant across the radius of the fuel and a value of 250 J kg^{-1} K^{-1} was used in conjunction with measurements reported by Matzke et al. [34] on SIMFUEL. Figure 27 and Figure 28 show similar trends in the evolution of thermal diffusivity and conductivity from the center of the pellet towards the periphery. From $r/r_p = 0$ to $r/r_p = 0.4$ thermal conductivity and thermal diffusivity remain constant within the uncertainty of the measurements. From $r/r_p = 0.45$ to $r/r_p = 1$ both properties exhibit a gradual decrease.

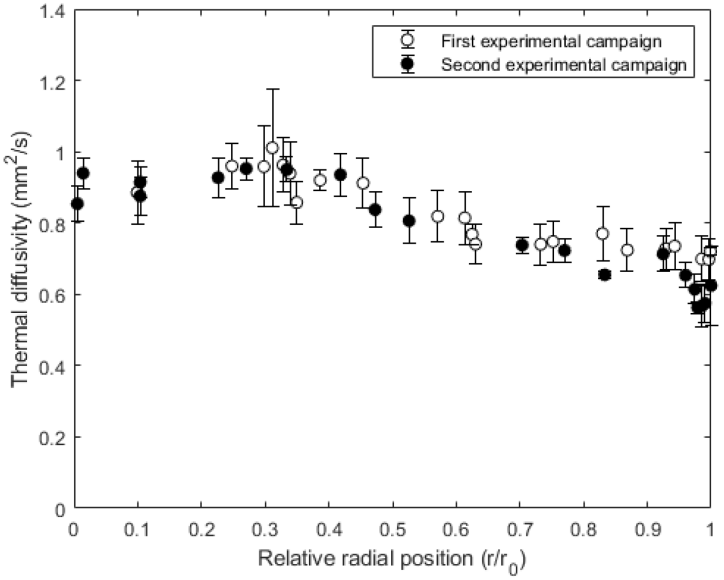

Figure 27. Radial profile of the measured thermal diffusivity of the sample from Rod A08.

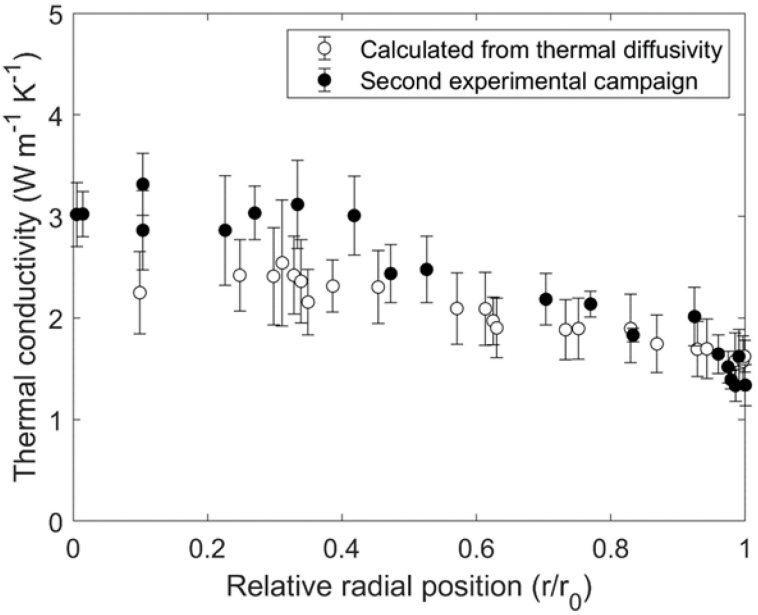

Figure 28. Radial profile of the thermal conductivity of the sample from Rod A08. The white circles are the values derived from the measured thermal diffusivity. The black circles are the measurements obtained from the TCM.

For the laser-flash measurements, an attempt was made to obtain a full cross-section slice from the original ceramography sample from Rod A08, but the amount of material left was not sufficient to obtain a good sample. Therefore, a specimen was cut from the sister Rod P16. Thermal conductivity has been calculated from the measured diffusivity values and correlations for specific heat and density available in the open literature. The density correlation provided by Spino, et al. [33] has been used to correct for the effects of burnup while the thermal expansion and specific heat correlations have been taken from

Fink et al. [35]. Figure 29 and Figure 30 show the evolution of thermal diffusivity and thermal conductivity, respectively, as a function of temperature. Upon heating, a gradual decrease in both thermal conductivity and thermal diffusivity is observed with increasing temperature. Upon cooling the measured values of these properties remain identical from 1000°C to 500°C. As the temperature is further decreased from 500°C to 100°C it can be observed that the sample exhibits higher thermal diffusivity and thermal conductivity values when compared to the heating results.

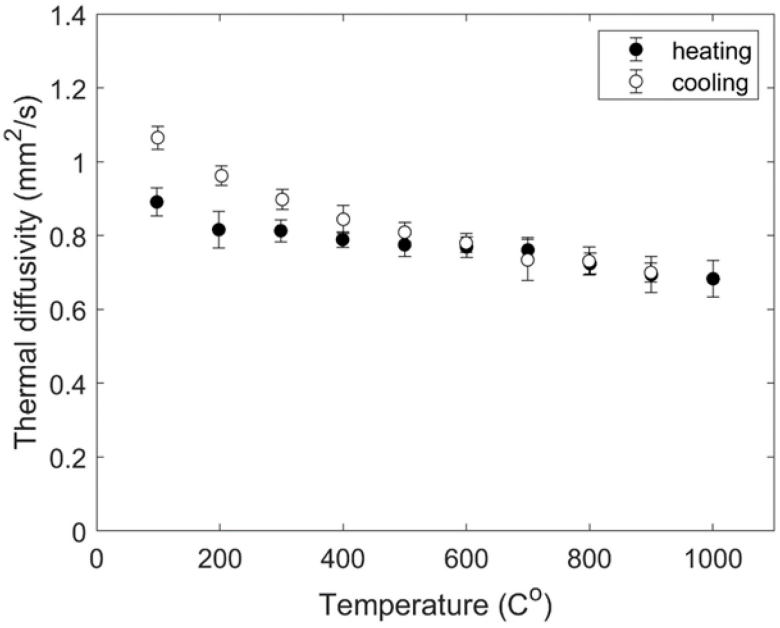

Figure 29. Thermal diffusivity versus temperature of a UO_2 sample from Rod P16. The black and white circles represent measurements performed upon heating and cooling, respectively.

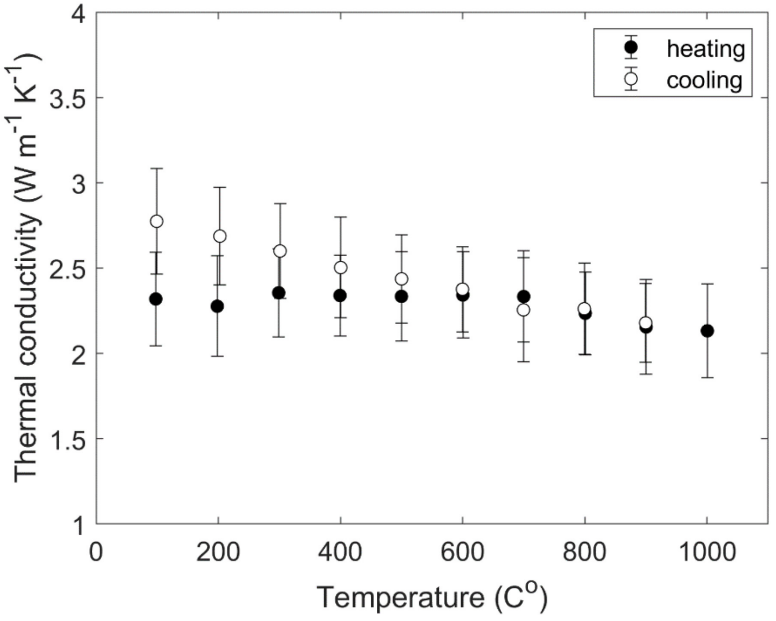

Figure 30. Thermal conductivity versus temperature of a UO_2 sample from Rod P16. The black and white circles represent measurements performed upon heating and cooling, respectively.

4. DISCUSSION

The non-destructive integral rod PIE proved a good performance of the rods, with comparable performance to the performance of other M5® rods [10]. The fission gas release values are also in line with the literature data compiled for high-power, high burnup rods, fitting the trend proposed by Manzel et al. [36] (Figure 4). By combining the Xe EPMA measurements presented in Figure 9 and Figure 10 with the pore characteristics presented in Figure 12 and Figure 13, some observations on the radial origin of the released gas can be made. As identified for the porosity, three major zones can be seen in the radial concentration of fission gas. The measured Xe profile in Figure 9 points out how the central part of the fuel till mid-radius ($r/r0 \approx 0.5$) has released all the local gas, suggesting that the large pores in the fuel center (Figure 13) have interconnected and released the gas. Passed the mid-radius, the drop in pore number and the steep increase in the local Xe inventory points out how in this second region the gas is still dissolved in the matrix or trapped in nanometric bubbles still accessible by the EPMA, which can probe a volume of a few cubic micron from the surface. The drop in the Xe signal between $r/r0 = 0.65$ and $r/r0 = 0.9$ is harder to interpret. The Xe X-ray maps such as the one shown in Figure 10 prove that at least part of the gas is confined in the bubbles, but it cannot be excluded that partial release has occurred, particularly in the intermediate zone between $r/r0 = 0.7–0.8$ preceding the HBS formation. Finally, the Xe signal drops due to the formation of HBS micrometric bubbles, as commonly observed in EPMA measurements in the HBS [18,37–39]. The determination of the radial gas concentration in the pellet is extremely important to address which regions in the pellet could be prone to bubble pressurization-driven fragmentation [5]. For this specimen, it can be expected that, in addition to the HBS, the intermediate radial region could experience fragmentation, being the retained gas quantity comparable to the produced inventory. The nanometric bubbles that were not opened by the FIB preparation were surrounded by a dense network of dislocations (Figure 21), which suggests that the pressure is high, close to the dislocation punching pressure.

In addition to the radial inventory of the gaseous fission products, assessment of the distribution of the volatiles (e.g., Cs and Te) is also important since it has been speculated that the volatilization of those species could contribute to the bubble pressurization during accidents [40]. It is interesting to note the correspondence between the Xe release in the central part of the fuel in Figure 9 and the depletion of Cs at the same radial locations in Figure 11. On the contrary, the local distribution of Cs and Xe at peripheral radial positions $r/r0 > 0.70$ are different. As discussed, the majority of the Xe migrates to nanometric bubbles or HBS bubbles as observed in Figure 10, Figure 20, and Figure 21, while Cs remains in the matrix. Walker's et al. [41] proposed that the two species would be both volatile at high temperature and share the same path of migration and release above 1200°C, while below those temperatures Cs would be liquid and could be stabilized in the matrix through reactions with uranium and fission products. Such considerations could explain the depletion of the two species observed in the central part of the pellet and the different localization of the two fission products in the colder regions of the pellet. The radial profile from Te is like the one from Cs, hence it is likely that Te was also in gaseous form and has been partially released from the central zones. Indeed, a large intergranular agglomerate of Te has been identified with the TEM (Figure 19), proving that Te migrates to intergranular cavities in the central areas of the fuel akin to fission gas. In the central region of the fuel, the so-called "gray phases" [24] were also observed (Figure 18). While those are commonly observed in SFR MOX fuels [42–44], they are less often observed in LWR fuels, unless the rod experienced a power transient [28]. The presence of large gray phases agglomerates and the extensive release of both Xe and volatile Cs and Te from the central zone suggest that the rod experienced high powers during part of the irradiation.

Regarding the grain structure across the pellet, a couple of observations can be made. At intragranular level, the amount of damage is substantial, which is reflected by the high density of intragranular dislocations (Figure 16a and b), but no clear trend can be established along the fuel radius outside the HBS, as all the measured values are comparable when the error is considered. The dislocation density is comparable with the measurements performed on other high burnup fuels [23] (Figure 17). The HBS grains are free of dislocation network and lines as expected in recrystallized grains, but still show small intragranular dislocation loops, as pointed out in Figure 16c. Those defects could be due to remaining damage from in-pile operation, but given the age of the fuel it could also be possible that they were formed due to decay damage while in storage [45]. The central region is characterized by grain subdivision, which continued from the pellet center till the mid-radius (Figure 14a, b, c, and d), where the presence of LAGB within the original grains abruptly stops (see Figure 14e and f). These observations, (i.e., the grain subdivision in the center and a sharp transition in the grain structure at $r/r0 \approx 0.50–0.55$) is analogous to what recently reported by Noirot et al. [46] on a 61 GWd/tHM-irradiated UO_2 sample. From the center to the mid-radius, there is a gradient in the amount of LAGB, which increases from the center to mid-radius, where it is the highest. The rising number of LAGB is highlighted by the increased local lattice distortion seen in the KAM maps in Figure 15. Such a behavior could be expected based on the local temperatures the fuel experienced. The temperature is higher moving towards the fuel center; therefore, thermal recovery is larger towards the central regions, which has partially annealed the defects responsible for the subgrain boundaries formation and results in less local distortion. The internal grain subdivision is absent in the second region of the pellet from mid-radius till the formation of the HBS, where the formation of the recrystallized submicrometric grains occurred. The nature of the subgrains in the central part of the pellet is different from the recrystallized grains in the HBS. In the central part of the pellet till mid-radius, the LAGB dominate (Figure 14d), while in the HBS the grain boundaries are mostly high angle [47]. Such observations are in line with previous works [46,47], who also observed restructuring dominated by LAGB in the pellet center. The zone with subdivided grains corresponds well with the end of the central porous zone and might suggest an interdependence between precipitation of fission gas bubbles and grain subdivision. Preferential formation of submicrometric grains on pore surfaces has been documented by different authors [48–50], but it does not necessarily imply that a high density of pores is a needed precursor for grain subdivision. Recent separate-effect testing using swift heavy ion irradiation to simulate fission fragment damage have shown that the presence of bubbles is not a necessary condition to have grain subdivision [51]. Formation of subgrains has been shown in crept UO_2 after compression tests [52], and recovery mechanisms during creep processes in the central part of the pellet could have played a role in the microstructure configuration. The discussed release of volatile fission products and the precipitation of gray-phases, which are generally observed only in ramped LWR oxide fuels, corroborate the hypothesis that this part of the pellet experienced high-irradiation temperatures, at least for part of the operation. Those could have favored a more ductile behavior of the fuel in the central zone and explain the formation of LAGB as a recovery mechanism driven by mechanical deformation rather than accumulation of radiation damage as it occurs in the peripheral region of the pellet [53]. The restructuring does not occur between $r/r0 \sim 0.5$ and the HBS formation as neither the dynamic recovery mechanism nor the irradiation-induced polygonization is acting at sufficient level in these intermediate regions to cause grain subdivision. At this stage, these remarks remain speculative, but extension of such analyses to other specimens and more details on the irradiation history will help to understand the formation mechanisms of this microstructure.

Figure 27 and Figure 28 show constant thermal diffusivity and thermal conductivity as a function of radius from the pellet center to the pellet mid-radius followed by a gradual decrease in these properties towards the pellet periphery. This trend is consistent with the measured inventory of fission gases such as Xe, which precipitate in nanometric bubbles with a limited quantity present in matrix solution in a three vacancy Schottky cluster. Such bubbles and point defects are effective phonon scattering sites and contribute to degradation of the thermal conductivity. Furthermore, the accelerated decrease in thermal diffusivity and conductivity towards the pellet periphery is in line with the significant increase in porosity

and burnup. Figure 29 and Figure 30 show a gradual decrease in thermal diffusivity and conductivity upon heating. This is consistent with the phonon-phonon scattering mechanism which becomes dominant in non-metals such as UO_2 with increasing temperature. Upon cooling, below 500°C, the thermal diffusivity and conductivity of the examined UO_2 sample exhibit higher values compared to the measurements obtained upon heating. An additional phonon scattering mechanism contributing to the degradation of thermal conductivity at lower temperatures is phonon-defect scattering. The recovery of thermal conductivity upon cooling is consistent with annealing/recombination of defects during the heating cycle. The increased mobility of point and extended defects at higher temperatures leads to defect annihilation and a resulting reduction in defect concentrations. The diminished defect population leads to a reduction in defect-phonon scattering rates and an increase in the thermal conductivity of the material.

The results of room temperature nanoindentation on fresh UO_2 fuels shows hardness values between 9.5 and 12.5 GPa [31,54,55] depending on the microstructure and manufacturing route of the UO_2. In this work at room temperature, the hardness varies between 6 and 12 GPa depending on the location of the indent. The Young's modulus for fresh UO_2 fuels measured with nanoindentation is in the range of 200 and 244 GPa again depending on the microstructure and manufacturing pathway. In this work here on the irradiated fuel it can be observed that the elastic modulus ranges between 93 and 181 GPa, depending on the radial location in the pellet. The porosity seems to be the dominant factor affecting the radial profiles of the Young's modulus and hardness, as the trends are opposite to the measured porosity (Figure 22 and Figure 23). Porosity strongly affects the load-bearing capabilities of a material; hence, it is understandable that the mechanical properties are largely influenced by the radial porosity profile.

The Young's modulus of irradiated UO_2 has been measured with a variety of techniques, including nanoindentation [56], acoustic microscopy [57,58], or a combination of acoustic microscopy and microhardness [59], all at room temperature. The values of the Young's modulus as a function of the local burnup measured from EPMA are compared with the literature values from References [56, 58] in Figure 31. The current data agree well with other measurements obtained from nanoindentation, while remain lower than the values measured by acoustic microscopy. The reason for the discrepancy is presently unknown.

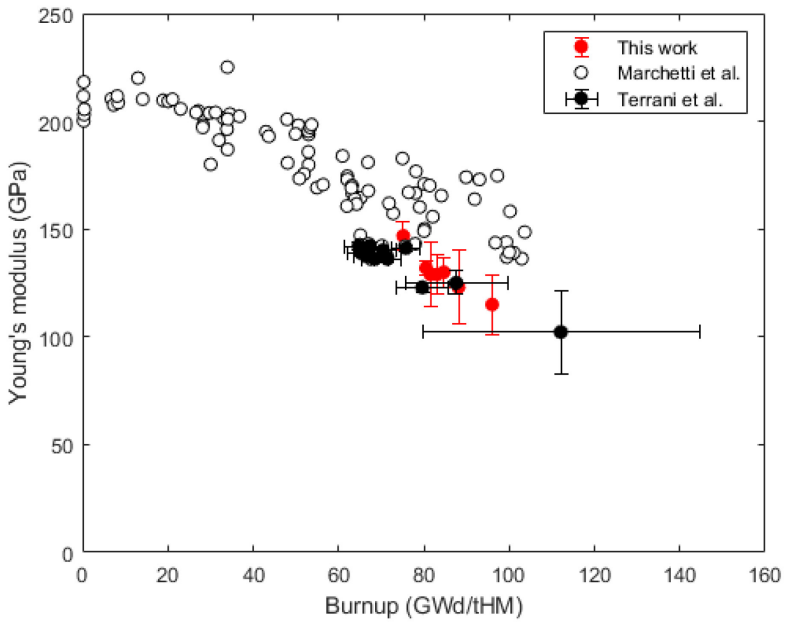

Figure 31. Young's modulus measured at room temperature as a function of local burnup. Literature values are also shown in the figure.

Most of the creep measurements performed on UO_2 are on fresh fuel at the macro-scale above 1000°C at low loads. The nanoindentation creep measurements performed here are slightly different as they are at lower temperatures and relativity high loads. The nanoindentation creep measurements were performed at 300°C and 500°C. There is one nanoindentation creep study performed on fresh UO_2 with different microstructures that could be used for comparison with these results. In Figure 32 the nanoindentation creep results from this study are compared with those of the fresh fuel form Frazer et al. [31].

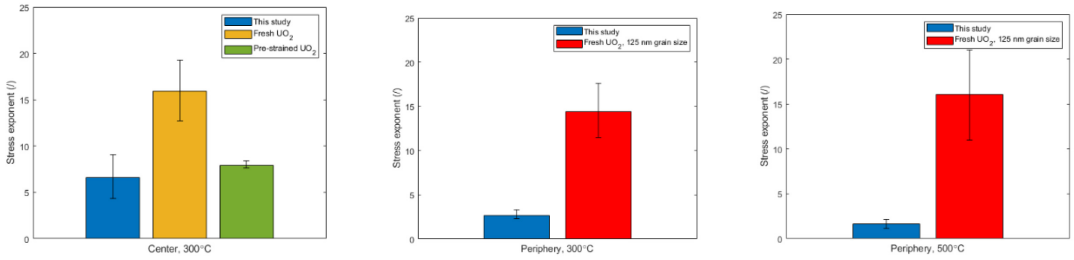

(a) (b) (c)

Figure 32. The comparison of the stress exponents measured on the irradiated fuel with those measure on fresh UO_2 [31] with different microstructures. (a) The center region of the pellet at 300°C, the periphery at (b) 300°C and 500°C.

The stress exponent measured in this study at 300°C in the central part of the pellet on the irradiated UO_2 is significantly lower than the fresh fuel, which was manufactured by conventional sintering route with roughly ~ 10 µm grain size and ~ 95% of the theoretical density (Figure 32a). The value of irradiated fuel is more similar to the stress exponent measured in a pre-strained sample, which was manufactured with the same characteristics of the fresh material, but it was also compressed at 1200°C to introduce deformation into the material before creep testing. The stress exponent for both the pre-strained sample and the irradiated UO_2 would suggest that the materials are deforming by dislocation glide in the material. The pre-straining and irradiation would introduce defects into the material enabling the deformation to occur more easily than in the fresh material. Indeed, the TEM data have shown a considerable number of dislocations in the irradiated fuel (Figure 17). The fresh material, instead, does not present a significant amount of dislocation, hence creep is not occurring, as proven by the stress exponent above 10. The values measured at the pellet periphery are compared in Figure 32b and c to a UO_2 surrogate spark plasma sintered with grain size 125 nm. At both temperatures, the deformation mechanism of the irradiated material is significantly different from the fresh material. While the fresh material has practically no creep, the periphery of the irradiated fuel would deform by dislocation glide at 300°C similarly to the center of the pellet. At 500°C, the stress exponent would indicate that grain boundary sliding is the dominant mechanism of deformation. Deformation of UO_2 by grain boundary sliding has been observed at much higher temperatures than the current study [60]. Grain size reduction due to the HBS formation and presence of defects and precipitates could influence the temperature range at which the mechanism is active and favor grain boundary sliding at temperatures lower than previously observed. Future testing on additional material would help in determining whether the current observation is a common feature of all high burnup fuels.

5. CONCLUSIONS

Comprehensive PIE has been conducted on a high burnup fuel to characterize the fuel microstructure and key properties such as thermal conductivity and mechanical properties. The determination of the distribution of fission gas, volatiles, and grain structure is a necessary pre-requisite to interpret the transient testing results and to establish the materials properties degradation at high burnup. Along the entire fuel radius, the amount of intragranular damage was substantial, with tangled networks of dislocation present within the grains at each radial location examined. Three major zones were identified within the pellet: (1) a central area till r/r0 ≈ 0.55 characterized by grain subdivision by polygonization, complete release of fission gas and volatile fission products such as Cs and porosity between 2% to 4%, (2) an intermediate region from r/r0 ≈ 0.55 till r/r0 ≈ 0.75–0.80 with low porosity and absence of grain subdivision, which retained almost all the locally produced gas and (3) the rim region with the exponential increase of porosity and grain subdivision typical of the HBS formation. Based on the local fission gas inventory, in addition to the HBS, the intermediate regions could be prone to fragmentation driven by bubble pressurization, in contrast to the central part that has been depleted of gas. The grain subdivision in the pellet central areas and the abrupt interruption of the subdivision at mid-radius are analogous to other studies performed on other samples with similar burnup [46, 47]. Although no definitive conclusion can be drawn on the mechanism driving this restructuring outside the rim, it can be postulated that the grain subdivision is a consequence of dynamic recovery at high temperature, which could have also favored gas release during deformation in-pile. The experimental evidence gathered here constitutes the baseline set of data that will help interpreting safety testing results of this material.

The formation of various zones with different grain size and porosity characteristics, as well as the precipitation of other fission products, has impact on the measured mechanical and thermal properties. The room temperatures of Young's modulus and hardness along the fuel radius showed a profile presenting three zones, reflecting the three areas identified by microscopy. Porosity, in particular, had a strong influence on those two properties. Room temperature Young's modulus and hardness were lower than previously measured with acoustic microscopy, but agreed well with other data obtained from nanoindentation, highlighting a technique-dependence of the measured values. The increase in temperature caused a decrease in both properties, as expected due to softening of the material. The most notable result was the determination of a much more pronounced creep behavior of the irradiated fuel compared to the as-fabricated material. The current values agree better with the data from pre-strained material, highlighting the important effect of irradiation defects (i.e., dislocation) in determining the deformation behavior. The dataset is still too limited to provide a robust correlation, but the study sets the path for future experimental campaigns.

Thermal diffusivity and thermal conductivity decreased from the pellet center to the pellet periphery. The degradation in thermal conductivity is consistent with the increase in porosity, fission gas concentration (Xe) and burnup from the pellet center towards the pellet periphery. Upon heating the thermal diffusivity and thermal conductivity were found to gradually decrease as a function of temperature which is consistent with phonon-phonon scattering in UO_2. Upon cooling an increase in thermal diffusivity and thermal conductivity was observed below 500°C, which is in line with the recombination of radiation induced defects during the prior heating cycle, which in the future could be confirmed by additional post-heating TEM.

The current studies employed a broad variety of advanced techniques that thoroughly evaluated the properties of high burnup fuel, providing a comprehensive description of the irradiation-induced modifications occurring at high burnup. These data will be valuable inputs to any integral and semi-integral results interpretation, as well as source for meso-scale models to describe performance of high burnup fuels.

6. REFERENCES

[1] Fuketa. T. 2012. *2.22 - Transient Response of LWR Fuels (RIA)*, in: R.J.M.B.T.-C.N.M. Konings (Ed.), Elsevier, Oxford: 579–593. https://doi.org/10.1016/B978-0-08-056033-5.00044-6.

[2] Nagase, F. 2012, *2.23 - Behavior of LWR Fuel During Loss-of-Coolant Accidents*. in: R.J.M.B.T.-C.N.M. Konings (Ed.), Elsevier, Oxford: 595–608. https://doi.org/10.1016/B978-0-08-056033-5.00045-8.

[3] Flanagan, M., A. Oberlander, B. C., Puranen. 2013. "Fuel fragmentation and dispersal under LOCA conditions: experimental observations." *TopFuel 2013*.

[4] Bianco, A., C. Vitanza, M. Seidl, A. Wensauer, W. Faber, R. Macián-Juan, 2015. "Experimental investigation on the causes for pellet fragmentation under LOCA conditions." *J. Nucl. Mater.* vol. 465: 260–267. https://doi.org/10.1016/j.jnucmat.2015.05.035.

[5] Kulacsy, K. 2015. Mechanistic model for the fragmentation of the high-burnup structure during LOCA *J. Nucl. Mater.* vol. 466: p. 409–416. https://doi.org/10.1016/j.jnucmat.2015.08.015.

[6] Turnbull, J. A., S. K. Yagnik, M. Hirai, D. M. Staicu, C. T. Walker. 2015. "An Assessment of the Fuel Pulverization Threshold During LOCA-Type Temperature Transients *Nucl. Sci. Eng.* vol. 179: 477–485. 10.13182/NSE14-20.

[7] Capps, N., Y. Yan, A. Raftery, Z. Burns, T. Smith, K. Terrani, K. Yueh, M. Bales, K. Linton, 2020. "Integral LOCA fragmentation test on high-burnup fuel." *Nucl. Eng. Des.* vol. 367: 110811. https://doi.org/10.1016/j.nucengdes.2020.110811.

[8] Jernkvist, L. O. 2019. "Modelling of fine fragmentation and fission gas release of UO2 fuel in accident conditions." *EPJ Nucl. Sci. Technol.* vol. 5. https://doi.org/10.1051/epjn/2019030.

[9] Jernkvist, L. O. 2020. "A review of analytical criteria for fission gas induced fragmentation of oxide fuel in accident conditions." *Prog. Nucl. Energy*. vol. 119: 103188. https://doi.org/10.1016/j.pnucene.2019.103188.

[10] Garner, G. L., B. A. Hilton, E. Mader, 2007. "Performance of Alloy M5® Cladding and Structure", in: *Proceedings of the 2007 International LWR Fuel Performance Meeting*, San Francisco.

[11] Klinger, M. 2017. "More features, more tools, more CrysTBox." *J. Appl. Crystallogr.* vol. 50. 10.1107/S1600576717006793.

[12] Adkins, C. A., T. R. Pavlov, S. C. Middlemas, R. S. Schley, M. C. Marshall, M. R. Cole. 2019. *Demonstrate Thermal Property Measurement on Irradiated Fuel in IMCL*. INL/EXT-19-55902. Idaho National Laboratory.

[13] Hurley, D. H., Z. Hua, R. S. Schley, 2018. *Closeout Phase II Qualification of the Thermal Conductivity Microscope for IMCL*. INL/EXT-18-51198. Idaho National Laboratory.

[14] Middlemas, S., Z. Hua, V. Chauhan, W.T. Yorgason, R. Schley, A. Khanolkar, M. Khafizov, D. Hurley, 2020. "Determining local thermal transport in a composite uranium-nitride/silicide nuclear fuel using square-pulse transient thermoreflectance technique." *J. Nucl. Mater.* vol. 528: 1–11. 10.1016/j.jnucmat.2019.151842.

[15] Hurley, D., R. Schley, 2017. *Enter TCM and Associated Equipment into Stage One Mockup.* Idaho National Laboratory.

[16] Z. Hua, H. Ban, M. Khafizov, R. Schley, R. Kennedy, D.H. Hurley, Spatially localized measurement of thermal conductivity using a hybrid photothermal technique *J. Appl. Phys.* **111** (2012) p. 1–7. 10.1063/1.4716474.

[17] Pakarinen, J., M. Khafizov, L. He, C. Wetteland, J. Gan, A. T. Nelson, D. H. Hurley, A. El-Azab, T. R. Allen. 2014. "Microstructure changes and thermal conductivity reduction in UO2 following 3.9 MeV He2+ ion irradiation." *J. Nucl. Mater.* vol. 454: 283–289. 10.1016/j.jnucmat.2014.07.053.

[18] Manzel, R., C. T. Walker, 2002. "EPMA and SEM of fuel samples from PWR rods with an average burn-up of around 100 MWd/kgHM," *J. Nucl. Mater.* vol. 301: 170–182. https://doi.org/10.1016/S0022-3115(01)00753-X.

[19] Garat, V., D. Deuble, B. Dunn, J. P. Mardon, 2012. "Quantification of the margins provided by M5 cladding in accidental conditions." *TopFuel 2012*, European Nuclear Society, Manchester, United Kingdom.

[20] Mardon, J. P., D. and S. J. Charquet. 2000. "Influence of composition and fabrication process on out-of-pile and in-pile properties of M5 alloy." *Zirconium in the Nuclear Industry: 12th Int. Symp. ASTM STP 1354*, G.P. Sabol, G.D. Moan (Eds.), American Society for Testing and Materials: 505–524.

[21] Finkeldei, S. 2019. "EPMA and TEM Characterization of a UO2 fuel pellet and cladding interaction layer."

[22] Spino, J., K. Vennix, M. Coquerelle, 1996. "Detailed characterisation of the rim microstructure in PWR fuels in the burn-up range 40–67 GWd/tM." *J. Nucl. Mater.* vol. 231: 179–190. https://doi.org/10.1016/0022-3115(96)00374-1.

[23] Nogita, K., K. Une, 1994. "Radiation-induced microstructural change in high burnup UO2 fuel pellets." *Nucl. Instruments Methods Phys. Res. Sect. B Beam Interact. with Mater. Atoms*. vol. 91: 301–306. https://doi.org/10.1016/0168-583X(94)96235-9.

[24] Kleykamp, H. 1985. "The chemical state of the fission products in oxide fuels." *J. Nucl. Mater.* vol. 131: 221–246. https://doi.org/10.1016/0022-3115(85)90460-X.

[25] Bramman, J. I., R. M. Sharpe, D. Thom, G. Yates, 1968. "Metallic fission-product inclusions in irradiated oxide fuels." *J. Nucl. Mater.* vol. 25: 201–215. https://doi.org/10.1016/0022-3115(68)90045-7.

[26] Kleykamp, H. 1979. "The chemical state of LWR high-power rods under irradiation." *J. Nucl. Mater.* vol. 84: 109–117. https://doi.org/10.1016/0022-3115(79)90154-5.

[27] Adenis, C., V. Langer, O. Lindqvist, 1989. "Reinvestigation of the structure of tellurium." *Acta Crystallogr. Sect. C*. vol. 45: 941–942. https://doi.org/10.1107/S0108270188014453.

[28] Thomas, L. E., C. E. Beyer, L. A. Chariot, 1992. "Microstructural analysis of LWR spent fuels at high burnup." *J. Nucl. Mater.* vol. 188: 80–89. https://doi.org/10.1016/0022-3115(92)90457-V.

[29] Oliver, W. C., G. M. Pharr, 1992. "An improved technique for determining hardness and elastic modulus using load and displacement sensing indentation experiments." *J. Mater. Res.* vol. 7: 1564–1583. DOI: 10.1557/JMR.1992.1564.

[30] Su, C., E. G. Herbert, S. Sohn, J. A. LaManna, W. C. Oliver, G. M. Pharr, 2013. "Measurement of power-law creep parameters by instrumented indentation methods." *J. Mech. Phys. Solids*. vol. 61: 517–536. https://doi.org/10.1016/j.jmps.2012.09.009.

[31] Frazer, D., B. Shaffer, B. Gong, P. Peralta, J. Lian, P. Hosemann, 2021. "Elevated Temperature Nanoindentation Creep Study of Plastically Deformed and Spark Plasma Sintered UO_2." *J. Nucl. Mater.* vol. 545: 152605. https://doi.org/10.1016/j.jnucmat.2020.152605.

[32] Roberts, J. T. A. 1974. "Mechanical equation of state and high-temperature deformation (≥0.5Tm) of uranium dioxide." *Acta Metall.* vol. 22: 873–878. https://doi.org/10.1016/0001-6160(74)90053-4.

[33] Spino, J., J. Rest, W. Goll, C. T. Walker. 2005. "Matrix swelling rate and cavity volume balance of UO2 fuels at high burn-up." *J. Nucl. Mater.* vol. 346: 131–144. https://doi.org/10.1016/j.jnucmat.2005.06.015.

[34] Matzke, H., P. G. Lucuta, R. A. Verrall, J. Henderson. 1997. "Specific heat of UO2-based SIMFUEL." *J. Nucl. Mater.* vol. 247: 121–126. https://doi.org/10.1016/S0022-3115(97)00069-X.

[35] Fink, J. 2000. "Thermophysical properties of uranium dioxide," *J. Nucl. Mater.* vol. 279: 1–18. 10.1016/S0022-3115(99)00273-1.

[36] Manzel, R., M. Coquerelle.1997. "Fission gas release and pellet structure at extended burnup." *Light Water Reactor Fuel Performance*, ANS, Portland, Oregon: 463–470.

[37] Noirot, J., L. Desgranges, J. Lamontagne, 2008. "Detailed characterisations of high burn-up structures in oxide fuels." *J. Nucl. Mater.* vol. 372: 318–339. https://doi.org/10.1016/j.jnucmat.2007.04.037.

[38] Walker, C. T. 1999. "Assessment of the radial extent and completion of recrystallisation in high burn-up UO_2 nuclear fuel by EPMA." *J. Nucl. Mater.* vol. 275: 56–62. https://doi.org/10.1016/S0022-3115(99)00108-7.

[39] Mogensen, M., J. H. Pearce, C. T. Walker. 1999. "Behaviour of fission gas in the rim region of high burn-up UO_2 fuel pellets with particular reference to results from an XRF investigation. *J. Nucl. Mater.* vol. 264: 99–112. https://doi.org/10.1016/S0022-3115(98)00474-7.

[40] Energy, O. N. 2016. *Report on fuel fragmentation, relocation and dispersal*. NEA/CSNI/R(2016)16. OECD-NEA.

[41] Walker, C. T., C. Bagger, M. Mogensen. 1996. "Observations on the release of cesium from UO_2 fuel." *J. Nucl. Mater.* vol. 240: 32–42. https://doi.org/10.1016/S0022-3115(96)00477-1.

[42] Kleykamp, H. 1988. "The Chemical State of Fission Products in Oxide Fuels at Different Stages of the Nuclear Fuel Cycle." *Nucl. Technol.* vol. 80:. 412–422. 10.13182/NT88-A34065.

[43] Sato, I., H. Furuya, T. Arima, K. Idemitsu, K. Yamamoto. 1999. "Behavior of fission products zirconium and barium in fastreactor fuel irradiated to high burnup *J. Nucl. Sci. Technol.* vol. 36: 775–780.

[44] O'boyle, D. R., F. L. Brown, J. E. Sanecki. 1969. "Solid fission product behavior in uranium-plutonium oxide fuel irradiated in a fast neutron flux." *J. Nucl. Mater.* vol. 29: 27–42. https://doi.org/10.1016/0022-3115(69)90124-X.

[45] Wiss, T., J.-P. Hiernaut, D. Roudil, J.-Y. Colle, E. Maugeri, Z. Talip, A. Janssen, V. Rondinella, R.J.M. Konings, H.-J. Matzke, W.J. Weber, Evolution of spent nuclear fuel in dry storage conditions for millennia and beyond *J. Nucl. Mater.* vol. 451 (2014) p. 198–206. https://doi.org/10.1016/j.jnucmat.2014.03.055.

[46] Noirot, J., I. Zacharie-Aubrun, T. Blay, Focused ion beam–scanning electron microscope examination of high burn-up UO2 in the center of a pellet *Nucl. Eng. Technol.* vol. 50 (2018) p. 259–267. https://doi.org/10.1016/j.net.2017.12.002.

[47] Gerczak, T. J., C. M. Parish, P. D. Edmondson, C. A. Baldwin, K. A. Terrani. 2018. "Restructuring in high burnup UO2 studied using modern electron microscopy." *J. Nucl. Mater.* vol. 509: 245–259. https://doi.org/10.1016/j.jnucmat.2018.05.077.

[48] Spino, J., D. Baron, M. Coquerelle, A. D. Stalios. 1998. "High burn-up rim structure: evidences that xenon-depletion, pore formation and grain subdivision start at different local burn-ups." *J. Nucl. Mater.* vol. 256: 189–196.

[49] Cappia, F. 2017. "Investigation of very high burnup UO_2 fuels in Light Water Reactors." *Technischen Universität München*.

[50] Lozano, N., L. Desgranges, D. Aymes, J. C. Niepce. 1998. "High magnification SEM observations for two types of granularity in a high burnup PWR fuel rim." *J. Nucl. Mater.* vol. 257: 78–87. https://doi.org/10.1016/S0022-3115(98)00056-7.

[51] Cappia, F., M. Cullison, T. Chen, B. Kombaiah, K. Bawane, F. Teng, J. Madden, E. Perez, T. Yao, P. Lei, J. Lian, Y. Miao, K. Mo. 2021. "Grain subdivision and structural modifications by high-energy heavy ions in UO_2 with different initial grain size." *Nucl. Instruments Methods Phys. Res. Sect. B Beam Interact. with Mater. Atoms*. **Accepted**.

[52] Iltis, X., N. Gey, C. Cagna, A. Hazotte, P. Sornay. 2015. "Microstructural evolution of uranium dioxide following compression creep tests: An EBSD and image analysis study." *J. Nucl. Mater.* vol. 456: 426–435. https://doi.org/10.1016/j.jnucmat.2014.10.005.

[53] Matzke, H., M. Kinoshita, 1997. "Polygonization and high burnup structure in nuclear fuels." *J. Nucl. Mater.* vol. 247: 108–115. https://doi.org/10.1016/S0022-3115(97)00081-0.

[54] Frazer, D., B. Maiorov, U. Carvajal-Nuñez, J. Evans, E. Kardoulaki, J. Dunwoody, T. A. Saleh, J. T. White. 2021. "High temperature mechanical properties of fluorite crystal structured materials (CeO_2, ThO2, and UO_2) and advanced accident tolerant fuels (U_3Si_2, UN, and UB_2). *J. Nucl. Mater.* vol. 554: 153035. https://doi.org/10.1016/j.jnucmat.2021.153035.

[55] Gong, B., D. Frazer, T. Yao, P. Hosemann, M. Tonks, J. Lian. 2019. "Nano- and micro-indentation testing of sintered UO_2 fuel pellets with controlled microstructure and stoichiometry." *J. Nucl. Mater.* vol. 516: 169–177. https://doi.org/10.1016/j.jnucmat.2019.01.021.

[56] Terrani, K. A., M. Balooch, J. R. Burns, Q. B. Smith. 2018. "Young's modulus evaluation of high burnup structure in UO_2 with nanometer resolution *J. Nucl. Mater.* vol. 508: 33–39. https://doi.org/10.1016/j.jnucmat.2018.04.004.

[57] Laux, D., D. Baron, G. Despaux, A. I. Kellerbauer, M. Kinoshita. 2012. "Determination of high burn-up nuclear fuel elastic properties with acoustic microscopy." *J. Nucl. Mater.* vol. 420: 94–100. https://doi.org/10.1016/j.jnucmat.2011.09.010.

[58] Marchetti, M., D. Laux, L. Fongaro, T. Wiss, P. Van Uffelen, G. Despaux, V. V Rondinella. 2017. "Physical and mechanical characterization of irradiated uranium dioxide with a broad burnup range and different dopants using acoustic microscopy." *J. Nucl. Mater.* vol. 494: 322–329. https://doi.org/10.1016/j.jnucmat.2017.07.041.

[59] Cappia, F., D. Pizzocri, M. Marchetti, A. Schubert, P. Van Uffelen, L. Luzzi, D. Papaioannou, R. Macián-Juan, V. V Rondinella. 2016. "Microhardness and Young's modulus of high burn-up UO_2 fuel." *J. Nucl. Mater.* vol. 479: 447–454. https://doi.org/10.1016/j.jnucmat.2016.07.015.

[60] Armstrong, W.M., W. R. Irvine. 1964. "Creep of urania base solid solutions." *J. Nucl. Mater.* vol. 12: 261–270. https://doi.org/10.1016/0022-3115(64)90080-7.